

Top quark mass measurement in the lepton plus jets channel using full simulation

A.-I.Etiennevre, J.-P.Meyer, J.Schwindling

CEA-Saclay, Dapnia/Service de Physique des Particules, F-91191 Gif-sur-Yvette Cedex, France

Abstract

This note presents a study of the top mass measurement in the $l\nu bqqb$ channel using a full GEANT simulation and the ATHENA reconstruction software. Methods are presented to select the events, to measure the mass in both top decay sides and to combine the two sides in order to improve the overall performance.

Contents

1	Introduction	3
I	Jet energy calibration and selection	4
2	Jet energy precalibration	4
2.1	Jets definition	4
	Purely electromagnetic jets	4
	b-jets	4
	Light jets	4
2.2	Jets energy precalibration	4
	Light jets energy precalibration	5
	Light jets energy resolution	5
	b-jets energy calibration	5
3	Event selection	11
3.1	Preselection	11
3.2	Final selection	12
II	Top mass measurement using the hadronic top decay	15
4	In situ jet energy calibration	15
4.1	Preselection of the light jet pair candidates	15
4.2	In situ energy rescaling from mass constraint and choice of the light jet pair . . .	16
4.3	Hadronic W reconstruction	16
5	Choice of the b-jet associated to the hadronic W	17
6	Top mass measurement	18
6.1	Top mass reconstruction	18
6.2	Combinatorial background	18
6.3	Stability of the method	18

7	Systematic errors on the top mass measurement	20
7.1	p_T -jet cut	20
7.2	Jet cone size	20
7.3	E_T^{miss} cut	20
7.4	Jet energy scale	20
	b-jet energy scale	21
	In situ light jet energy scale	21
7.5	Electronic noise	21
7.6	Toy Monte Carlo study	21
III	Top mass measurement using the semi-leptonic top decay	29
8	The neutrino energy reconstruction	29
8.1	Study of the missing transverse momentum	29
8.2	The lepton-missing p_T transverse mass	31
8.3	Reconstruction of the neutrino p_z	39
9	The semi-leptonic top quark mass reconstruction	41
9.1	Combining the leptonic W with a b quark jet	41
9.2	Results on the reconstructed semi-leptonic top quark mass	42
9.3	Sensitivity to generated top quark mass	45
IV	Combining both top decays	46
10	Combining the W's with the b quark jets	46
11	Results on the reconstructed top quark mass	49
V	Conclusion	53
VI	Annex	54
12	Appendix 1: Electron identification.	54

1 Introduction

The aim of the study presented in this note is the measurement of the top mass in the ATLAS detector, in the lepton plus jets channel of the $t\bar{t}$ decay : each top quark decays almost exclusively into a W boson and a b-quark, one of the W bosons decays leptonically ($W \rightarrow l\nu$) and the other one hadronically ($W \rightarrow jj$).

This study has been performed with a sample of 500000 inclusive $t\bar{t}$ events generated using PYTHIA, including Final State Radiation (FSR) and a top mass equal to $175 \text{ GeV}/c^2$; they have been simulated with the full simulation of the ATLAS detector, in the initial configuration, for $|\eta| < 3.2$ (GEANT3) and reconstructed within the ATHENA framework (version 7.0.0). This corresponds roughly to 6 days of data taken by ATLAS at low luminosity. Jets have been reconstructed using the cone algorithm, for different cone sizes in order to determine the optimal one. The stability of the method with the top mass has been checked by using events generated at $m_{top} = 160 \text{ GeV}/c^2$, $170 \text{ GeV}/c^2$, $180 \text{ GeV}/c^2$ and $190 \text{ GeV}/c^2$.

This note is divided into four parts. The first part describes the jet energy precalibration and event selection common to the hadronic and leptonic sides. Parts 2 and 3 are devoted to the study of hadronic and leptonic top decays, respectively. The last part presents the combination of the two top quarks decays. Several sources of systematic errors on the top mass reconstruction have been investigated and are presented in parts 2,3 and 4.

Part I

Jet energy calibration and selection

2 Jet energy precalibration

2.1 Jets definition

Jet objects can be separated into three categories, described below : purely electromagnetic jets (rejected as jet candidates in our analysis), b-jets and light jets.

Purely electromagnetic jets

Electromagnetic particles (e^+ , e^- , γ) are usually also reconstructed as jet objects. Figure 1 shows the distribution of the distance ($\Delta R = \sqrt{\Delta\Phi^2 + \Delta\eta^2}$) between a given jet and the closest electromagnetic cluster versus the ratio between the cluster energy and the jet energy. A jet is labeled electromagnetic if this distance is below 0.2, and the energy ratio above 0.8. While $\simeq 76\%$ of the electrons have their closest jet indeed tagged as electromagnetic with these cuts, only 0.15 % of the other jets pass these cuts.

b-jets

The b-tagging algorithm was not implemented in the 7.0.0 ATHENA version; therefore, we made an artisanal b-jet definition, based on the distribution, shown on Figure 2, of the distance between a true b quark, coming from the decay of the corresponding top after gluon radiation, and the closest non-electromagnetic jet. The jet is tagged as a b-jet if this distance is smaller than 0.2. The efficiency of this tagging is equal to 92 %, thus much higher than a realistic b-tagging.

Light jets

The remaining jets, which are not purely electromagnetic jets and not b-tagged, are called light jets.

2.2 Jets energy precalibration

As explained in the next section, the event selection begins with a filter which consists in applying several cuts and among them, cuts on the jets transverse energy. Therefore, a precalibration of this energy needs to be performed at the first level of our analysis, for b-jets and light jets. This calibration relies on the Monte Carlo information for both jets. We study the difference between the jet energy and the corresponding true quark energy for b-jets, the corresponding Monte Carlo jet for light jets, as a function of energy, in bins of η^a . This is illustrated in this note with events reconstructed using a jet cone size equal to 0.4, but the determination of the precalibration factors has of course been performed separately for each studied cone size.

^aThe η region $[0; 2.5]$ has been divided into five ranges for this study : $|\eta| \leq 0.6$, $0.6 < |\eta| \leq 1$, $1 < |\eta| \leq 1.4$, $1.4 < |\eta| \leq 1.8$ and $1.8 < |\eta| \leq 2.5$: these ranges correspond to calorimetric regions where the behaviour is roughly constant.

Light jets energy precalibration

Figure 3 shows the difference between the energy of the light jet and the corresponding Monte Carlo jet energy^b as a function of Monte Carlo jet energy, for the five studied ranges in η . The calibration factors, function of energy and defined for each range in η , are given by a fit to these curves. Figure 4 shows the same variables, after calibration, integrating over all η values : the residual miscalibration is smaller than 1 GeV, except at very low energy, which is satisfactory given the value of the p_T jet cut applied later (at least 20 GeV).

Light jets energy resolution

Energy resolution follows from the calibration study described above : the distribution of the difference between the light jet energy and the corresponding Monte Carlo jet energy has been studied for several energy bins, and fitted by a gaussian whose width corresponds to the energy resolution. Figure 5 shows the behaviour of this resolution, as a function of energy of the light jet, for different η ranges : the resolution obtained here is comparable to the resolution given in the Physics TDR, above 200 GeV, but is much worse at smaller energy.

b-jets energy calibration

Energy calibration of b-jets has been performed by studying the difference between the b-jet energy and the corresponding initial (i.e. before any gluon radiation) b quark. Some of the b-quarks will decay semileptonically ($b \rightarrow l\bar{\nu}c$) with the neutrino undetected. If the lepton is an electron, it will be, most of the time, merged in the jet energy ; if it is a muon, it is not contained in the calorimeter and is reconstructed in the muon spectrometer. In the present algorithm, the muon is not added so the muon energy is missing in the jet energy. Since the muon is reconstructed, we can identify such events and calibrate them separately^c. The distribution of the distance ΔR between the b-jet and the closest reconstructed muon is shown in Figure 6 : we tag the b-decay as being muonic if ΔR is smaller than 0.2.

Figures 7 and 8 show the difference between the b-jet energy and the corresponding b quark energy as a function of the b quark energy, in five ranges in η and for both kinds of b decay. The calibration for muonic b decays is clearly different from the other b decays. The calibration factors, function of energy and defined for each range in η , are given by a fit to these curves. Figure 9 shows the same variables, after calibration, for any η value and any kind of b-decay : the miscalibration is smaller than 2 GeV.

^b Among the Monte Carlo jets, the one associated to a reconstructed jet is the closest one, provided the distance between the Monte Carlo jet and the jet is smaller than 0.2

^c We did not try to identify electrons in b-jets and to calibrate the corresponding jet separately

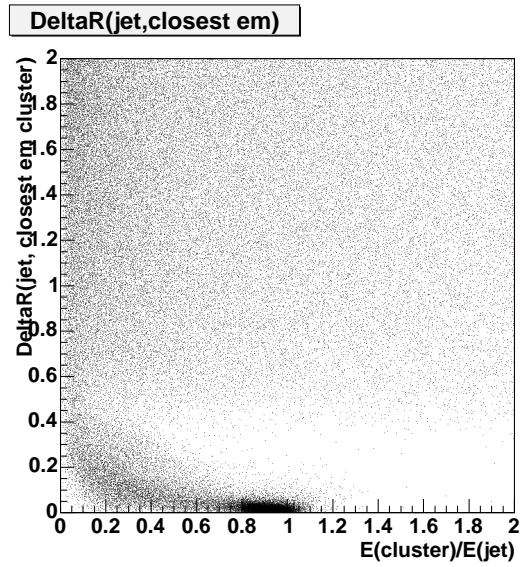


Figure 1: Distance (ΔR) between a jet and the closest electromagnetic cluster, versus the ratio $E(\text{cluster})/E(\text{jet})$

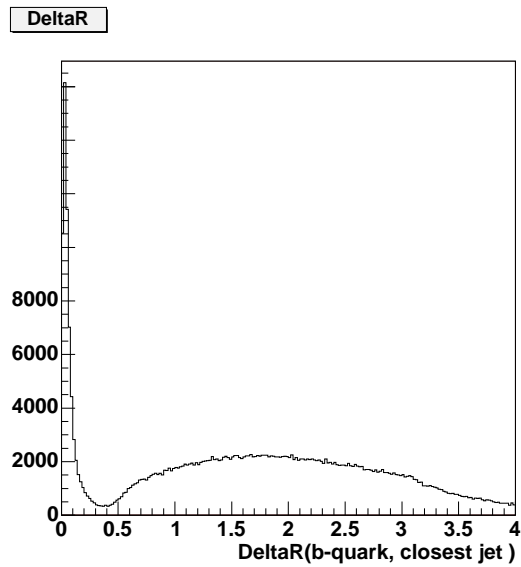


Figure 2: Distance (ΔR) between a b quark (Pythia information) and the closest non electromagnetic jet

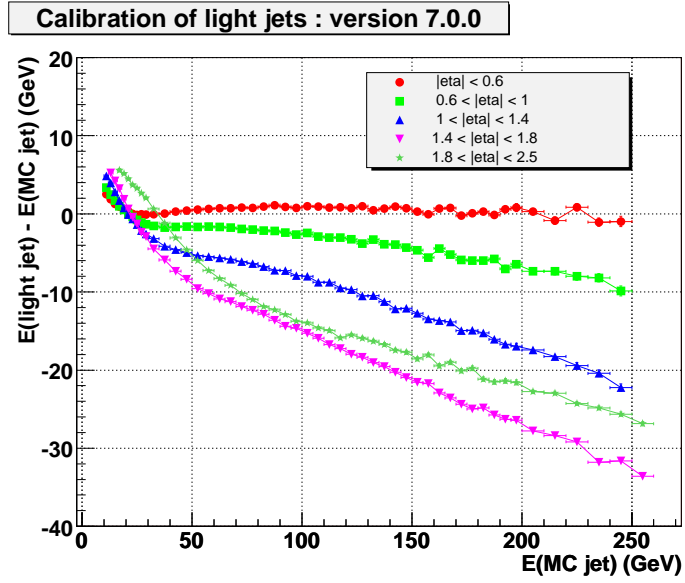


Figure 3: *Difference between the light jet energy and the corresponding Monte Carlo jet energy, as a function of the Monte Carlo jet energy and for different ranges in η*

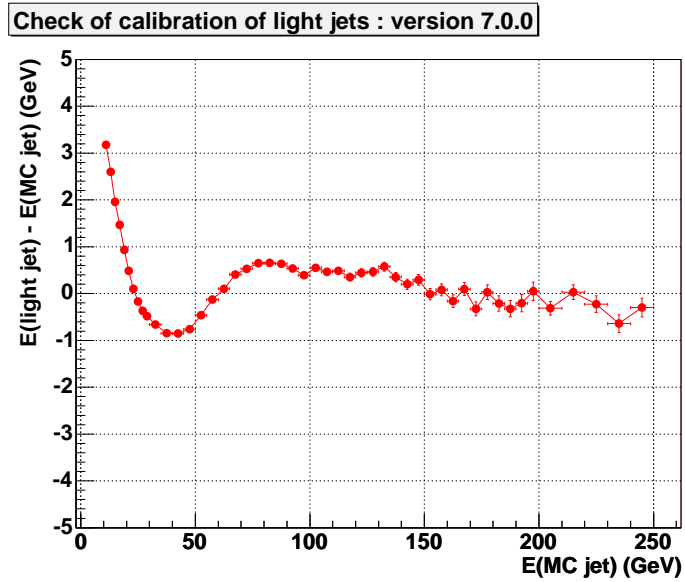


Figure 4: *Check of the light jet energy calibration*

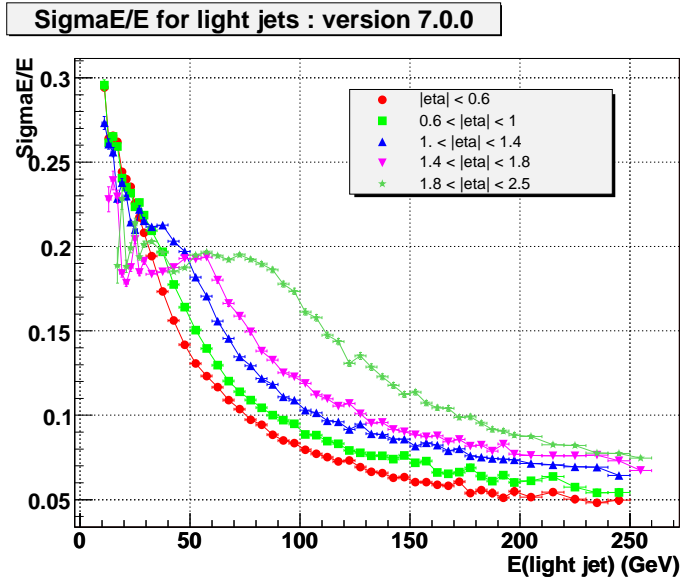


Figure 5: *Energy jet resolution for different η ranges*

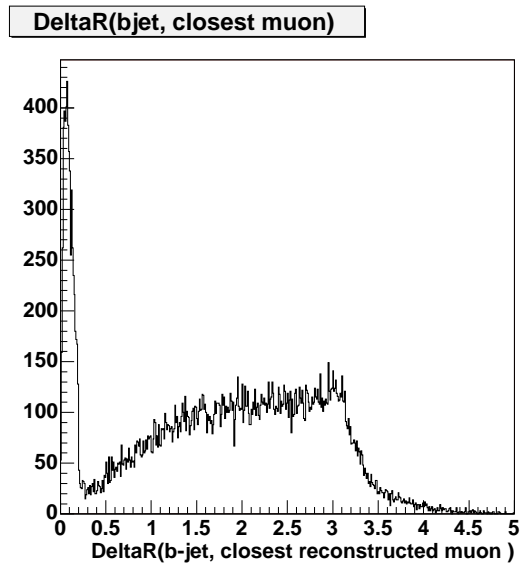


Figure 6: *Distance (ΔR) between a b -jet and the closest reconstructed muon*

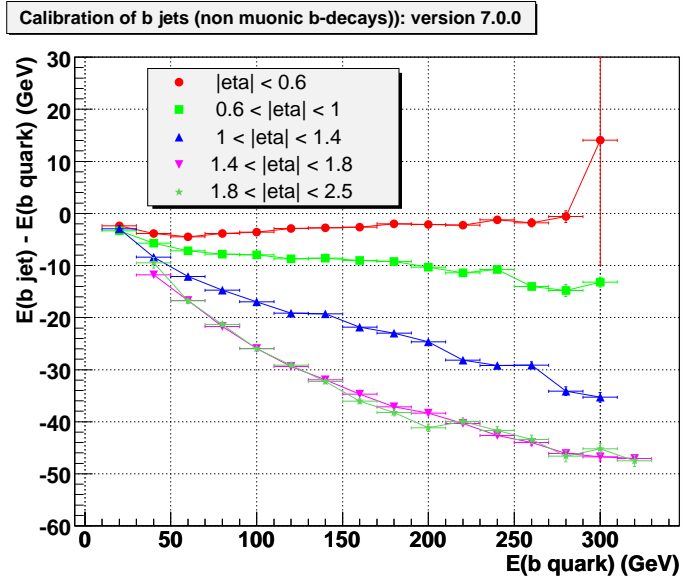


Figure 7: Difference between the b -jet energy and the corresponding b quark energy, as a function of the b quark energy and of η , for non muonic b -decays

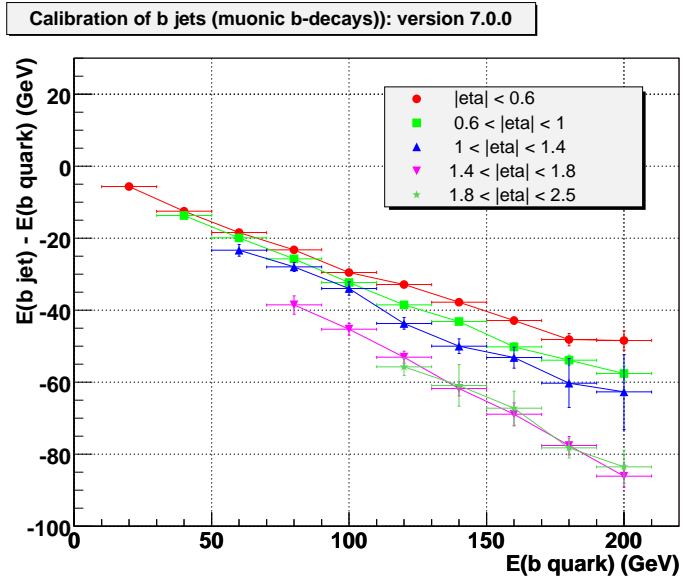


Figure 8: Difference between the b -jet energy and the corresponding b quark energy, as a function of the b quark energy and of η , for muonic b -decays

Check of calibration of b jets, version 7.0.0

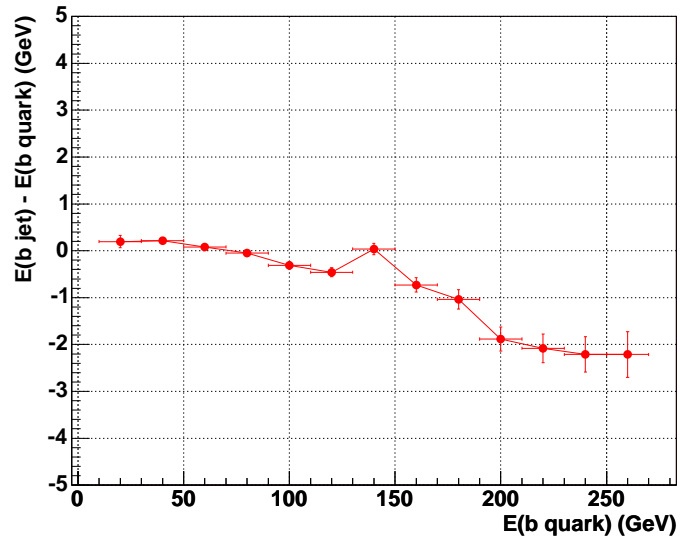


Figure 9: Check of the b-jet energy calibration

3 Event selection

The event selection ($t\bar{t} \rightarrow l\nu bjjb$ ($l = e, \mu$)) proceeds in two steps : a preselection is first performed in order to remove part of the fully hadronic $t\bar{t}$ decays and the semi-leptonic decays with a too small energy jet or lepton (background events). The final selection is then performed on the remaining events.

3.1 Preselection

The following cuts are applied:

- The missing tranverse energy, defined as the missing transverse momentum measured in the calorimeter minus the transverse momenta of the reconstructed muons, must be greater than 20 GeV. Figure 10 shows this distribution for all events (in white) and for the $t\bar{t} \rightarrow l\nu bjjb$ ($l = e, \mu$ or τ) decays (shaded).

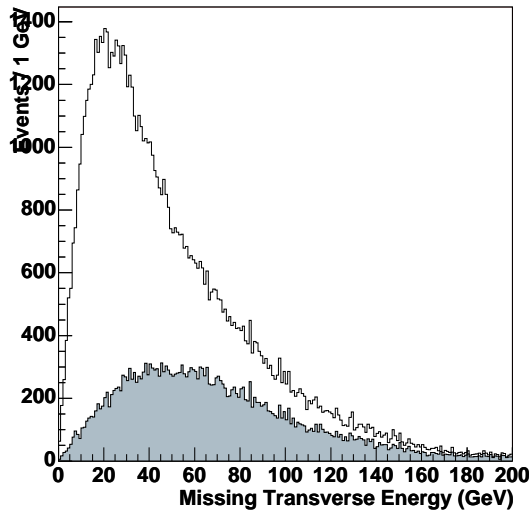


Figure 10: *Distribution of the missing transverse energy for all events (white histogram) and for the $t\bar{t} \rightarrow l\nu bjjb$ ($l = e, \mu$ or τ) decays (shaded)*

- There must be at least one reconstructed lepton with transverse momentum greater than 20 GeV and $|\eta| < 2.5$, where muons are identified as the tracks reconstructed by Muonbox, and electrons are identified as described in the appendix.

Figure 11 shows the distribution of the transverse momentum of the electron or muon in $e\nu bjjb$ and $\mu\nu bjjb$ events, hereafter called *signal events* (although some $\tau\nu bjjb$ events are also signal like).

- There must be at least 4 jets with $|\eta| < 2.5$ and a (pre-calibrated) transverse energy greater than 20 GeV (Figure 12).

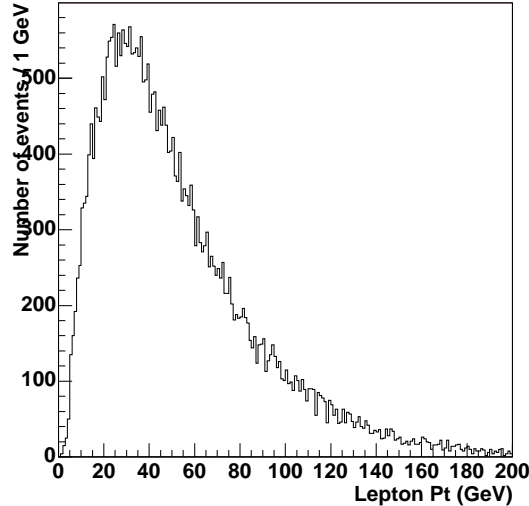


Figure 11: *Transverse momentum of the signal leptons (from KINE information)*

Table 1 gives the number of events after each cut, for the various final states. The initial number of events is lower than 500000 because of losses during reconstruction (either because of ATHENA crashes or because of CASTOR problems). The efficiency is the fraction of signal events passing the cuts. The purity is the fraction of signal events among the remaining top events.

cut	hadronic	$e\nu b j j b$	$\mu\nu b j j b$	$\tau\nu b j j b$	leptonic	total	efficiency (%)	purity (%)
no cut	266892	45983	46122	46094	21268	426359	100	21.6 ± 0.1
Etmiss	190066	42312	42953	42964	20122	338417	92.6 ± 0.1	25.2 ± 0.1
Nleptons	33139	27322	27445	7473	14269	109648	59.5 ± 0.2	49.9 ± 0.2
Njets	20709	17081	16834	4462	4277	63363	36.8 ± 0.2	53.5 ± 0.2

Table 1: *Number of events after each cut of the filter, for the various final states*

This filter keeps 14.9% of the events (reconstructed with a cone of $\Delta R = 0.4$): 7.8% of the hadronic events, 36.8% of the signal events, 9.7% of the events with one τ decay, and 20.1% of the 2-lepton decays. After the filter, 55% of the events are signal events.

The fraction of events kept by the filter and the signal efficiency increase slightly with the cone size, as shown in table 2, but the signal purity is slightly decreasing with cone size.

3.2 Final selection

The final selection proceeds as follows:

- about 40% of the remaining fully hadronic events are selected because of a leptonic decay of one of the b quarks. In order to reduce this background, the number of isolated leptons (with $p_T > 20$ GeV and $|\eta| < 2.5$) is required to be exactly one, with a lepton

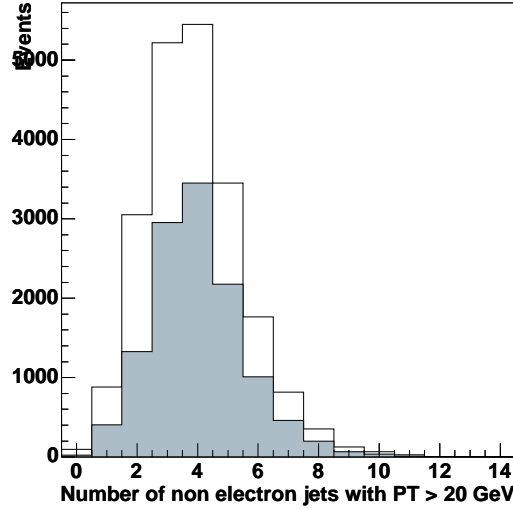


Figure 12: Number of jets with $P_T > 20$ GeV and $|\eta| < 2.5$ for all events (white histogram) and for the $t\bar{t} \rightarrow l\nu b j b$ ($l = e, \mu$ or τ) decays (shaded)

cone	fraction kept (%)	efficiency (%)	purity (%)
0.3	14.0	34.9	54.1
0.4	14.9	36.8	53.5
0.5	15.4	37.0	53.3
0.6	15.4	37.2	52.6

Table 2: Fraction of events kept by the filter, efficiency on the signal and purity, as a function of the cone size

being declared isolated if the distance to the closest (non-electron) jet is greater than 0.2. (Figure 13 shows the distribution of the distance between the electrons or the muons and the closest jet).

- there must be exactly 2 b jets, as defined in section 2, with $p_T > 20$ GeV and $|\eta| < 2.5$.

Table 3 shows the number of selected events after each cut for the various final state. The selection efficiency of signal events is about 18%, and the purity 68%. Table 4 gives the evolution of these numbers with cone size. The signal efficiency (and purity) decreases with an increasing cone size, mainly because of the isolation cut: the efficiency of the isolation cut on signal events is 79.6% for a 0.3 cone, and drops to 70.4% for a 0.6 cone.

Finally, the p_T cut on the jet energies (light jets and b jets) has been varied. The effect on the fraction of events kept by the selection is shown in table 5 for a 0.4 cone.

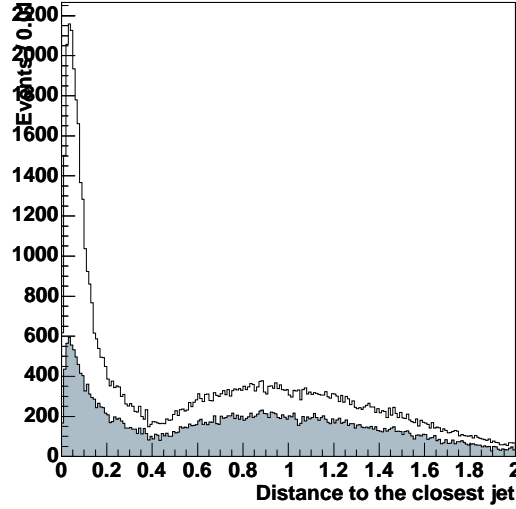


Figure 13: Distance between the leptons and the closest jet for all events (white histogram) and for the $t\bar{t} \rightarrow l\nu bj\bar{j}b$ ($l = e, \mu$ or τ) decays (shaded)

cut	hadronic	$e\nu bj\bar{j}b$	$\mu\nu bj\bar{j}b$	$\tau\nu bj\bar{j}b$	leptonic	total	efficiency (%)	purity (%)
filter	20709	17081	16834	4462	4277	63363	36.8 ± 0.2	53.5 ± 0.2
isolation	10923	13590	11969	2365	2765	41612	27.7 ± 0.1	61.4 ± 0.3
2 b jets	4414	8877	7977	1479	2066	24813	18.3 ± 0.1	67.9 ± 0.3

Table 3: Number of events after each cut of the final selection, for the various final states

cone	fraction kept (%)	efficiency (%)	purity (%)
0.3	6.1	19.3	68.2
0.4	5.8	18.3	67.9
0.5	5.2	16.2	67.2
0.6	4.5	13.9	65.8

Table 4: Fraction of events kept by the event selection, efficiency on the signal and purity, as a function of the cone size

P_T cut (GeV)	fraction kept (%)	efficiency (%)	purity (%)
20	5.8	18.3	67.9
30	3.6	11.5	69.6
40	1.9	6.2	70.0
50	0.9	3.0	69.5

Table 5: Fraction of events kept by the event selection, efficiency on the signal and purity, as a function of cut on the transverse momentum of the jets

Part II

Top mass measurement using the hadronic top decay

The top mass is determined from the reconstruction of the invariant mass of a three-jet system : the two light-jets from the W and one of the two b-jets. Results are presented using a jet cone size equal to 0.4 and a cut on the jet p_T equal to 40 GeV/c. The determination of this combination of three jets proceeds in two steps : the choice of the two light jets, explained in section 4, and the choice of the b-jet associated to the reconstructed hadronic W, explained in section 5. The top mass reconstruction obtained is described in section 6, and a non exhaustive study of systematic errors on this measurement is detailed in section 7.

4 In situ jet energy calibration

4.1 Preselection of the light jet pair candidates

Events kept after the selection described above have at least two light jets above a given threshold on their transverse momentum (50% of the events have more than two). Figure 14 shows the distribution of the invariant mass of the light jet pairs, made with events with only two light jets. In a first step, we select the hadronic W candidates in a mass window of $\pm 5\sigma_{m_{jj}}$ around the peak value of this distribution, where $\sigma_{m_{jj}}$ is the width of the fit performed (sum of a gaussian and a third order polynomial). The efficiency is then equal to 1.3 %.

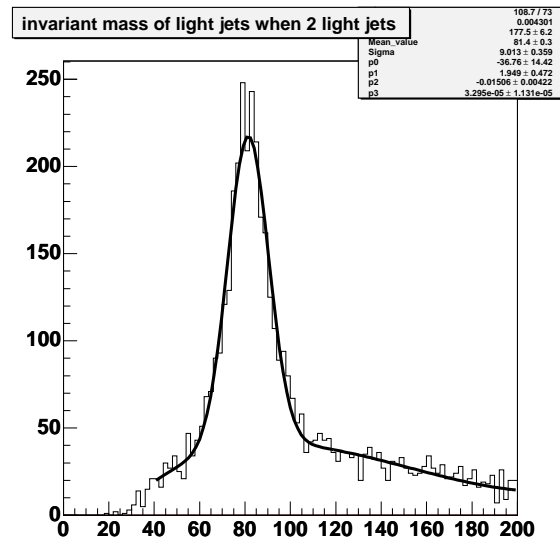


Figure 14: Invariant mass of light jets pair (p_T cut equal to 40 GeV, cone $\Delta R = 0.4$)

4.2 In situ energy rescaling from mass constraint and choice of the light jet pair

The accuracy on the top mass measurement is strongly correlated to the precision on the jet energy reconstruction, as will be shown later (7.4). In order to reduce the incidence of a light-jet energy mis-measurement (due to the energy lost out of cone) on the precision of the top mass measurement, an in-situ calibration of these jets is performed, through a χ^2 minimization procedure [1]. This minimization is applied event by event, for each light-jet pair combination. The expression of χ^2 , given by equation (1), is the sum of three terms : the first (and leading) one corresponds to the constrain of the jet pair invariant mass M_{jj} to the PDG W mass (M_W) ; the others correspond to the jet energy correction factors, α_i $i = 1, 2$, to be determined by this minimization (σ_i $i = 1, 2$ is the resolution on the light jet energy, determined as explained in section 2).

$$\chi^2 = \frac{(M_{jj} - M_W)^2}{\Gamma_W^2} + \frac{(E_{j1}(1 - \alpha_1))^2}{\sigma_1^2} + \frac{(E_{j2}(1 - \alpha_2))^2}{\sigma_2^2} \quad (1)$$

The χ^2 is minimized, event by event, for each light jet pair ; the light jet pair j_1, j_2 corresponding to the minimal χ^2 is kept as the hadronic W candidate. This minimization procedure also leads to the corresponding energy correction factors α_1, α_2 , whose distribution, as a function of the jet transverse momentum, is shown in figure 15 ; the width of the distribution of α decreases with energy, as expected.

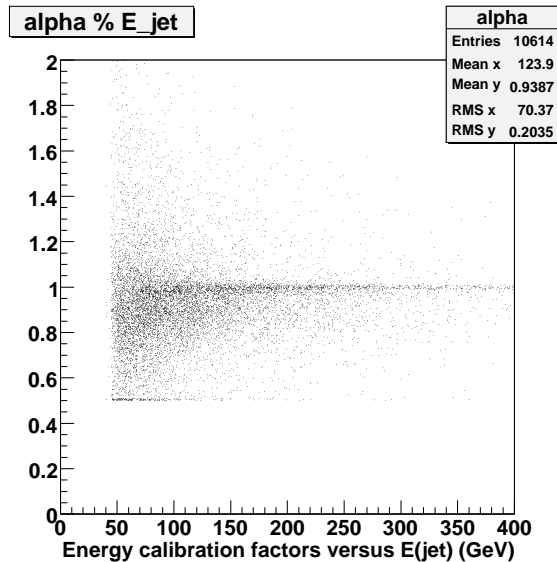


Figure 15: Distribution of the energy correction factor α_i , versus the transverse momentum p_T of the light jets, for a p_T cut equal to 40 GeV, and a cone size equal to 0.4

4.3 Hadronic W reconstruction

The hadronic W mass, reconstructed with the light jets chosen by this χ^2 minimization, is therefore very narrow, as illustrated in figure 16, since, given the jet energy resolution, the first

term in 1 dominates the χ^2 . Further on, we will consider only the hadronic W candidates which belong to a mass window of $\pm 2\Gamma_{m_W}$ ($\Gamma_{m_W} = 2.1$ GeV). The purity on the hadronic W is equal to 56% and the final efficiency, to 1.1%.

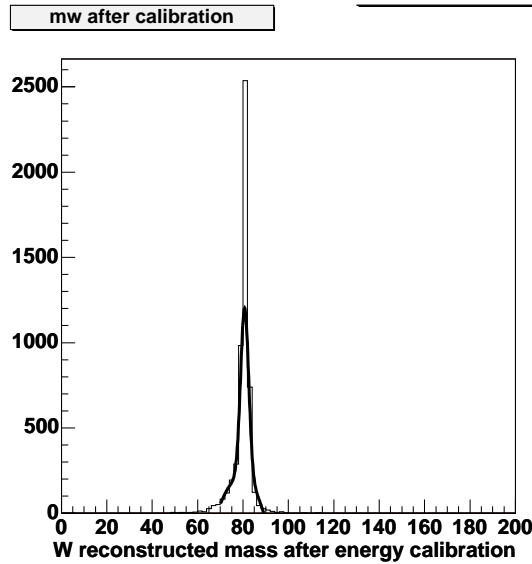


Figure 16: *Hadronic W mass (p_T cut equal to 40 GeV, and cone size equal to 0.4)*

5 Choice of the b-jet associated to the hadronic W

The next step in the top mass reconstruction is to associate one of the two b-jets in the event to the hadronic W candidate. Several methods have been studied ; in order to discriminate between them, we estimated the b-jet identification purity corresponding to each method, and chose the one giving the highest purity :

- b-jet leading to the highest p_T for the reconstructed top : purity equal to 75%
- b-jet closest to the reconstructed hadronic W (smallest ΔR) : purity equal to 74%
- b-jet closest to the reconstructed hadronic W (smallest angle between the W and the b-jet) : purity equal to 73%
- b-jet furthest to the reconstructed lepton : purity equal to 71%

Therefore, the b-jet associated to the reconstructed top is the one leading to the highest p_T for the top.

6 Top mass measurement

6.1 Top mass reconstruction

The reconstructed three jets (two light jets from the hadronic W and the chosen b-jet) invariant mass is shown in figure 17. The mass peak ($175.5 \pm 0.4 \text{ GeV}/c^2$) is in good agreement with the generated value ($175 \text{ GeV}/c^2$), for the $40 \text{ GeV}/c$ p_T cut ; the width is equal to $11.6 \pm 0.4 \text{ GeV}/c^2$. The corresponding efficiencies and purities are summarized in Table 6 (efficiencies could be lower with a realistic b-tagging). In a mass window around $\pm 3\sigma_{m_{top}}$, the total purity increases to 59.8%, whereas the efficiency is divided by a factor 2.

	Total efficiency (%)	b purity (%)	W purity (%)	Top purity (%)
full mass window	1.1	75.4	56.5	45.0
mass window within $\pm 3\sigma_{m_{top}}$	0.46	83.3	64.5	56.7

Table 6: Total efficiency and W , b and top purity of the final selected events (cone 0.4 and p_T cut = 40 GeV)

6.2 Combinatorial background

The existence of initial and final state radiation (ISR and FSR) leads to a higher jet multiplicity, and therefore to a combinatorial background, corresponding to a combination of three jets, with at least one jet wrongly associated to the hadronic W or to the b quark coming from the same top quark. The contribution of this background to the top mass distribution is shown in Figure 17.

6.3 Stability of the method

In order to check the stability of this top mass measurement, the same analysis has been applied to events generated with a top mass equal to $160 \text{ GeV}/c^2$, $170 \text{ GeV}/c^2$, $180 \text{ GeV}/c^2$ and $190 \text{ GeV}/c^2$. Results, summarized in Figure 18, show a linear dependence (with a slope close to 1) of the reconstructed top mass value on the generated top mass.

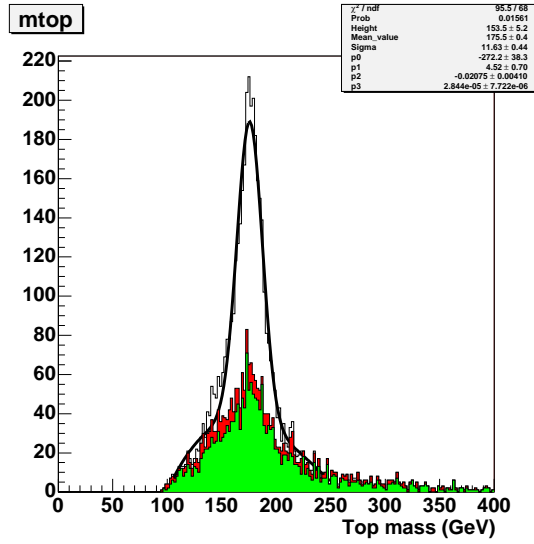


Figure 17: Contribution of the combinatorial background to the top mass distribution (in green, the contribution from wrong W combinations, and in red, from wrong W combinations or b -jet associations)

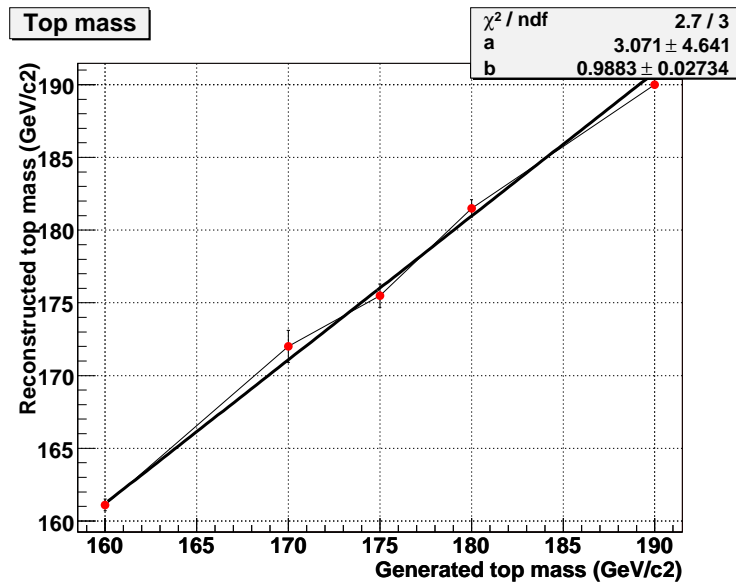


Figure 18: Reconstructed top mass versus generated top mass

7 Systematic errors on the top mass measurement

The results on the top mass measurement exposed above have been obtained with a jet cone size (ΔR) equal to 0.4 and a cut on the transverse momentum of the jets equal to 40 GeV/c. We explain in this section why these values are optimal for our analysis (7.1 and 7.2) ; this study will have to be finalized taking into account the behaviour of background events as a function of the jet cone size and p_T -jet cut. Several systematic errors have also been estimated, and are shown in this section (7.3,7.4,7.5 and 7.6).

7.1 p_T -jet cut

In order to determine the optimal value of these two parameters, we have studied the variation of the purities (on the hadronic W, on the corresponding b, and on the top) and of the final efficiency, as a function of the p_T -jet cut : this is summarized in Figures 19, 20, 21 and 22, obtained for a jet cone size equal to 0.4. Moreover, the value of the ratio $\frac{S}{B}$, not studied with full simulation but taken from the TDR, increases as the p_T jet threshold increases. We decided to take the value of 40 GeV for this threshold, as a good compromise between efficiency and purity. The final value has to be confirmed by studying the background with full simulation.

7.2 Jet cone size

Figures 23 and 24 show the energy calibration factors, for b-jets and light jets, for several cone sizes : miscalibration is smaller with larger cones, which is logical for b-jets, but not obvious for light jets as the calibration for these jets is based on the comparison between the jet energy and the Monte Carlo jet energy.

Purities and total efficiency depend on the jet cone size, as summarized in Figures 25, 26, 27 and 28. One origin of the differences between cone sizes is our way to perform b-tagging : therefore, this study will have to be redone with a realistic b-tagging.

7.3 E_T^{miss} cut

The E_T^{miss} cut applied (20 GeV), together with the request of one isolated lepton with a p_T greater than 20 GeV leads to an important background rejection, according to the study performed in the ATLAS TDR [2] : therefore, the E_T^{miss} cut is enough efficient. The sensitivity of this cut on our analysis has been evaluated for several values of E_T^{miss} , and is summarized in Table 7 : an increase of its value does not affect strongly the purities nor the efficiency, and the value of the reconstructed top mass is stable.

E_T^{miss} cut	Efficiency (%)	b purity (%)	W purity (%)	Top purity (%)	Top mass (GeV/ c^2)
20 GeV	1.1	56.5	75.4	45.0	175.5
25 GeV	1.0	56.4	75.5	44.6	175.4
30 GeV	0.9	56.1	75.9	44.7	175.4

Table 7: Total efficiency and W, b and top purity of the final selected events (cone 0.4 and p_T cut = 40 geV), for different values of the E_T^{miss} cut

7.4 Jet energy scale

In order to estimate the effect of the jet energy scale uncertainty, a miscalibration coefficient has been applied to the b-jet and light jet energies, separately.

b-jet energy scale

The linear dependence of the reconstructed top mass on the b-jet energy scale is shown in Figure 29. A 1% scale error on b-jet energies would induce a shift on the top mass equal to 0.6 GeV ; the studies performed with Atlfast gave a shift equal to 0.7 GeV.

In situ light jet energy scale

As an in-situ calibration is performed for the light jet energies, the effect of a light jet energy miscalibration is lower than the one estimated above. This is shown in Figure 30. A 1% scale error on light jet energies would induce a shift on the top mass equal to 0.15 GeV ; the studies performed with Atlfast gave a shift equal to 0.3 GeV.

7.5 Electronic noise

The effect of electronic noise on the mass measurement has been assessed by reconstructing the 175 GeV sample with electronic noise switched off, and computing the mass shift event by event, for all events in common in the final top mass distributions. This shift is shown in figure 31. There is a 1.4 GeV offset, perhaps due to a threshold in the cell energies. With a 0.4 cone, the contribution of electronic noise to the mass resolution is 4.4 GeV.

7.6 Toy Monte Carlo study

The variation of the reconstructed top mass as a function of the cut on jet transverse momenta is shown in figure 32. With the full reconstruction (blue squares), the mass increases by about 3 GeV from a 20 GeV cut to a 50 GeV cut. An increase is also observed in a toy simulation (red dots), where the true quark momenta are smeared by the jet energy resolution, although with a smaller amplitude.

We believe that the effect is mostly due to the resolution on the jet energies ; when applying a cut on their momenta, one selects jets with a high energy fluctuation and rejects jets with a low energy fluctuation. This leads to a shift of the mass towards higher values.

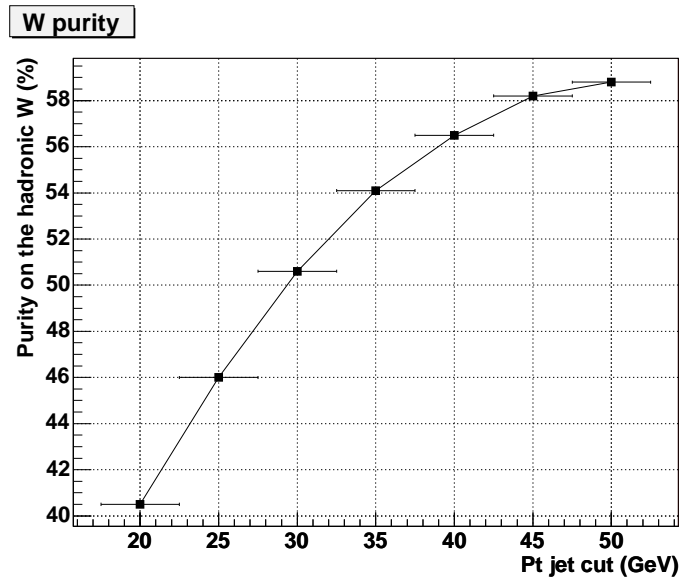


Figure 19: Hadronic W purity as a function of the p_T -jet cut, for a cone jet size equal to 0.4

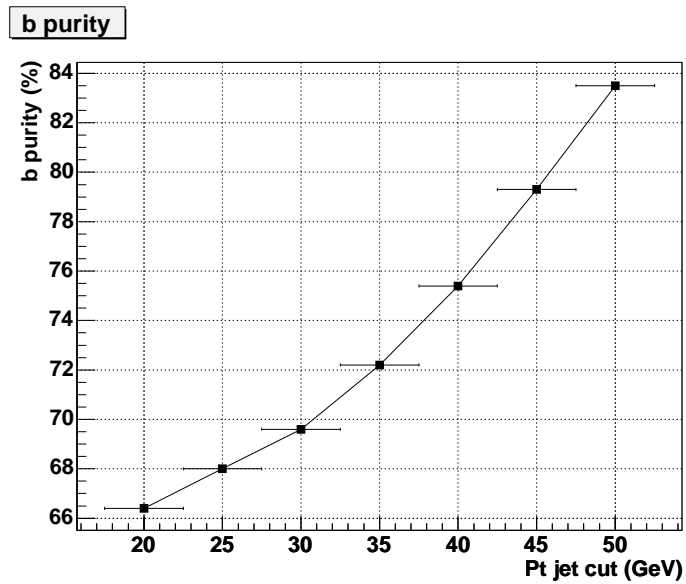


Figure 20: b purity as a function of the p_T -jet cut, for a cone jet size equal to 0.4

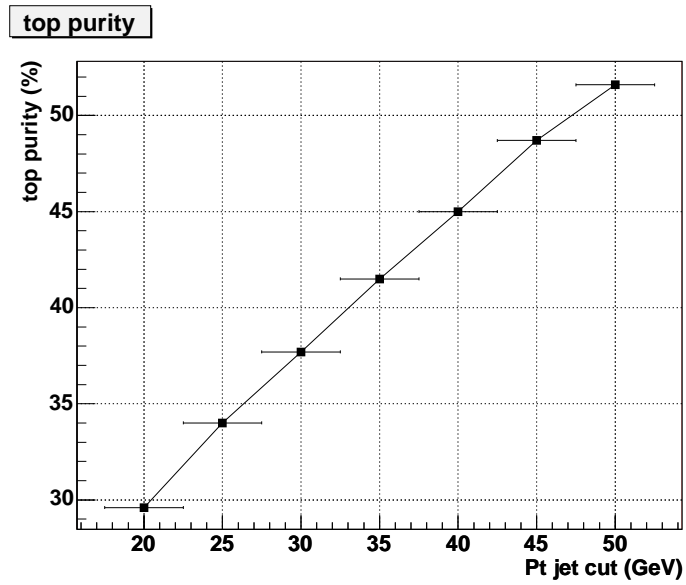


Figure 21: Top purity as a function of the p_T -jet cut, for a cone jet size equal to 0.4

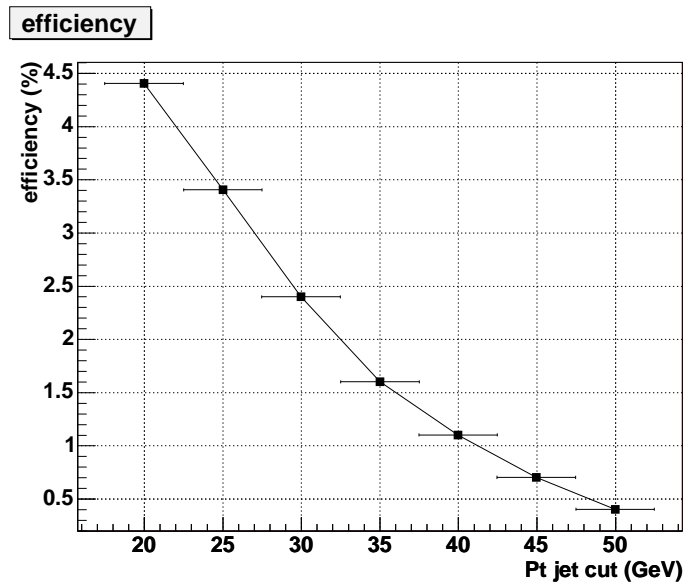


Figure 22: Final efficiency as a function of the p_T -jet cut, for a cone jet size equal to 0.4

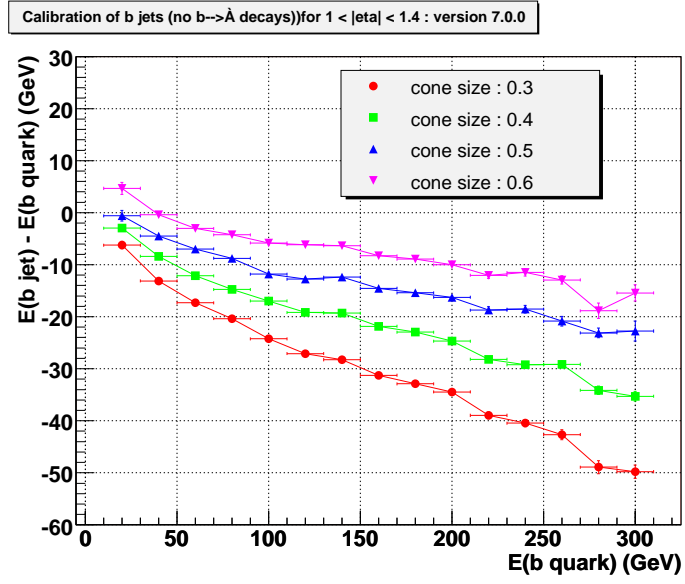


Figure 23: Energy calibration factor of b-jets, for different cone sizes $1 \leq |\eta| \leq 1.4$

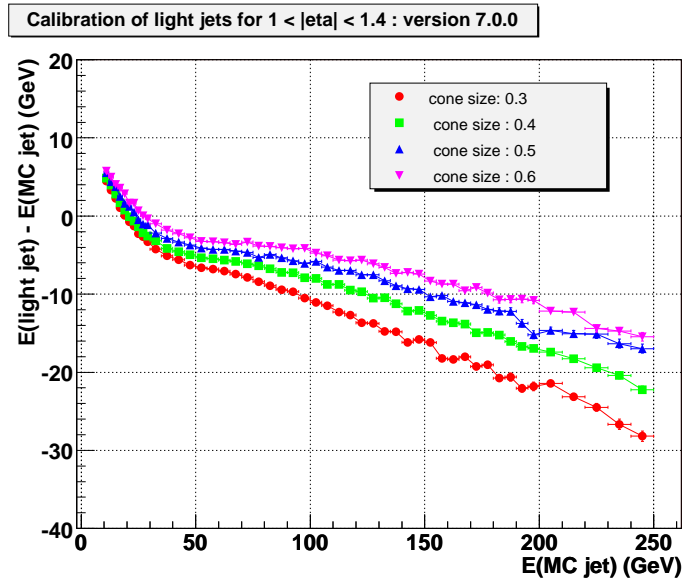


Figure 24: Energy calibration factor of light jets, for different cone sizes, and $1 \leq |\eta| \leq 1.4$

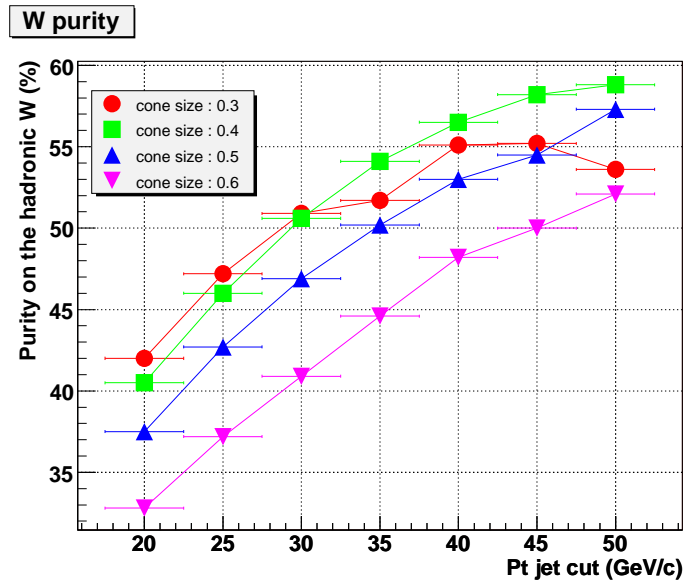


Figure 25: Hadronic W purity as a function of the p_T jet cut, for several cone jet sizes

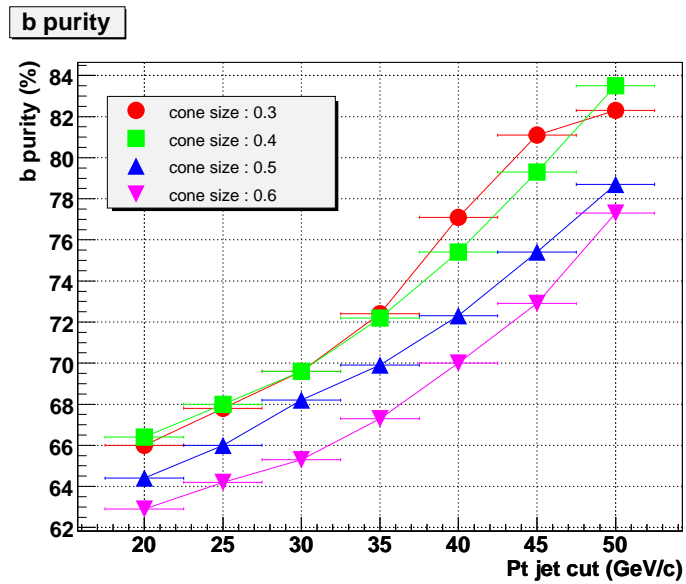


Figure 26: b purity as a function of the p_T jet cut, for several cone jet sizes

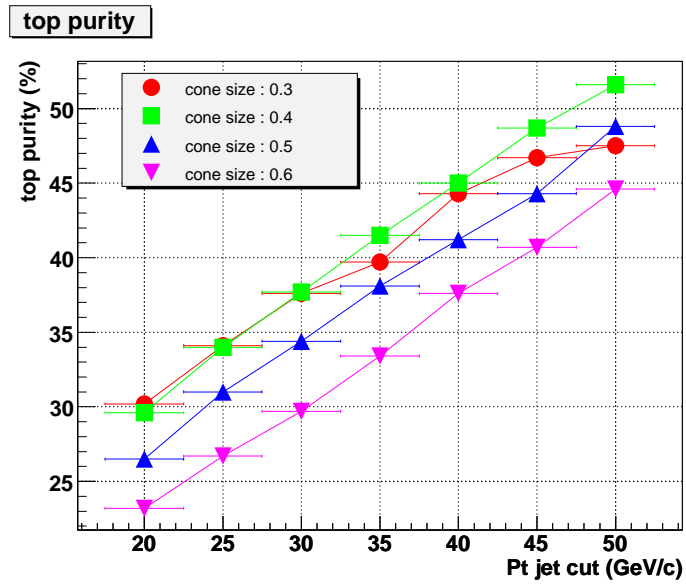


Figure 27: Top purity as a function of the p_T jet cut, for several cone jet sizes

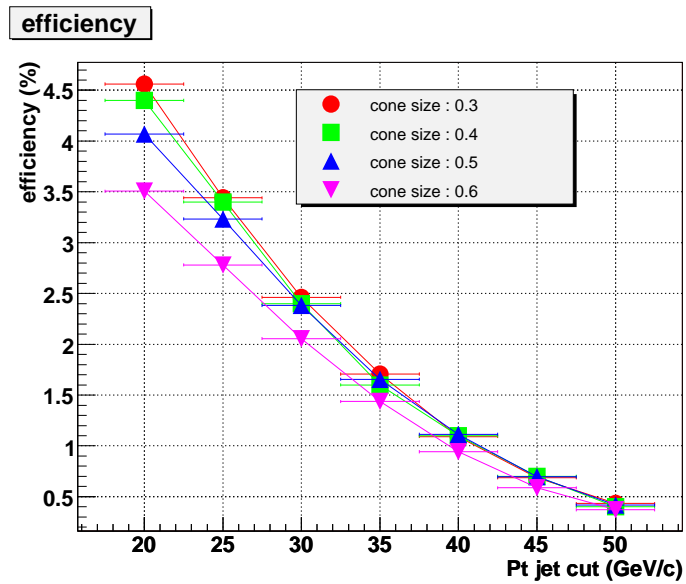


Figure 28: Final efficiency as a function of the p_T jet cut, for several cone jet sizes

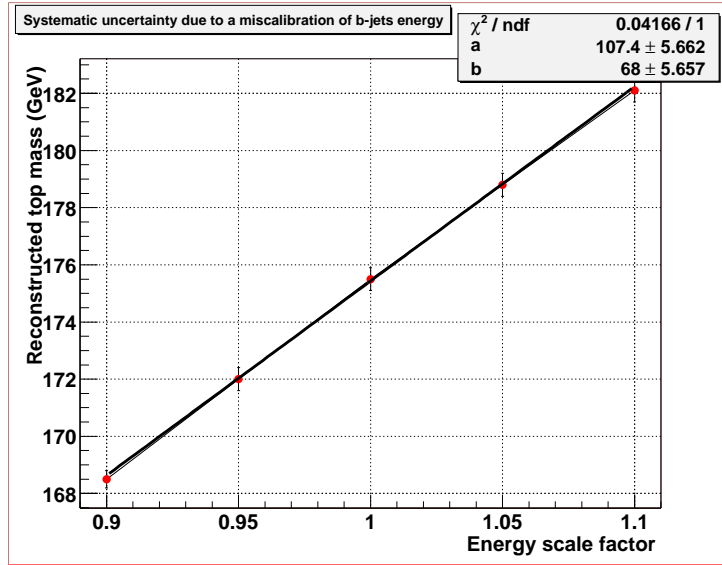


Figure 29: Reconstructed top mass (cone size 0.4 and p_T cut = 40 GeV) as a function of the b-jet energy scale

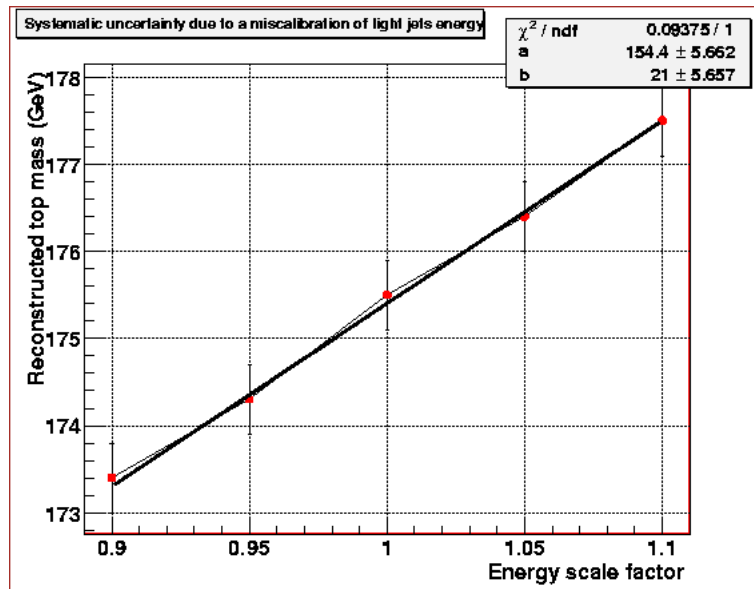


Figure 30: Reconstructed top mass (cone size 0.4 and p_T cut = 40 GeV) as a function of the light jet energy scale

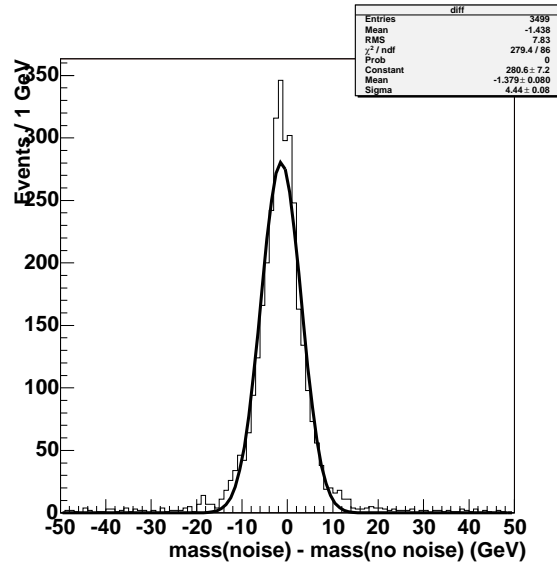


Figure 31: Shift of the top mass distribution due to the electronic noise in the calorimeters

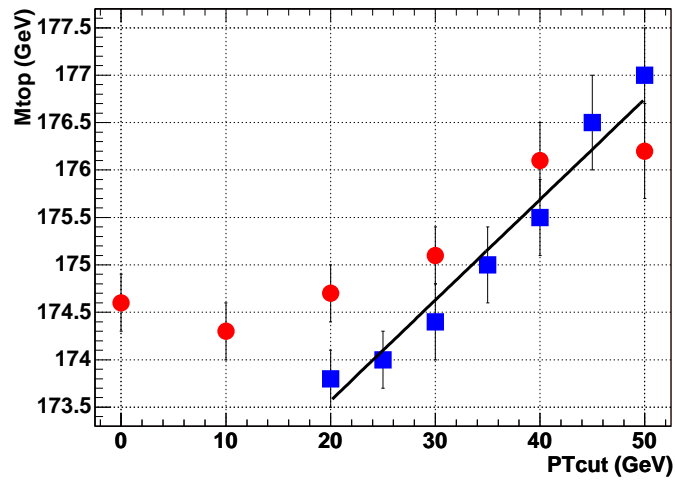


Figure 32: Reconstructed mass as a function of the cut on the jet transverse momenta. Blue dots are for the full simulation and reconstruction, red dots for a toy simulation.

Part III

Top mass measurement using the semi-leptonic top decay

In this part we will present an independent study of the semi-leptonic top decay using the same filtered events used for the hadronic top decay in the previous sections. If not mentioned otherwise, we use events generated with a top mass of 175 GeV/c².

8 The neutrino energy reconstruction

8.1 Study of the missing transverse momentum

In order to reconstruct the neutrino momentum we first have to work in the plane transverse to the beam axis. Summing up all the cell energies, the total transverse energy measured in the calorimeter is equal to 0, for a perfect calorimeter and in the absence of non-interacting particles (eg neutrinos) or partially contained particles (eg muons). For the latter we use the muon spectrometer behind the calorimeter to measure their momentum. Therefore we build our P_x^{miss} and P_y^{miss} variables in the following way:

$$P_x^{\text{miss}} = E_x^{\text{missH1}} - P_x^\mu$$
$$P_y^{\text{miss}} = E_y^{\text{missH1}} - P_y^\mu$$

where:

- E_x^{missH1} and E_y^{missH1} are the projection on the X and Y axes of minus the sum over calorimeter cell energies, using the H1 calibration.
- P_x^μ and P_y^μ are the projection on the X and Y axes of the sum of the reconstructed muon momenta.

In order to check the neutrino p_x and p_y resolution we compute (as recommended in the CBNT documentation for ATHENA 7.0.0) the quantities:

$$P_x^{\text{miss}} - (E_x^{\text{TrueFull}} - \text{True}P_x^\mu)$$
$$P_y^{\text{miss}} - (E_y^{\text{TrueFull}} - \text{True}P_y^\mu)$$

where:

- E_x^{TrueFull} and E_y^{TrueFull} are the projection on the x and y axes of $-\vec{E}_T$, the vector sum of all true energy deposits in the calorimeter.
- $\text{True}P_x^\mu$ and $\text{True}P_y^\mu$ are the projection on the x and y axes of the sum of the true muon momenta.

Figure 33 and Figure 34 show the resolution on the X and Y projections of the transverse missing momentum for the case where we selected only top-antitop events occurring with exactly one semi leptonic decay. The obtained resolution is around 16 GeV/c and the mean value is close to zero in both directions. If one uses the standard calibration instead of H1, the resolutions grow by 3 GeV/c but the mean values stay close to zero. For this reason we keep the H1 calibration in the P_x^{miss} and P_y^{miss} calculation.

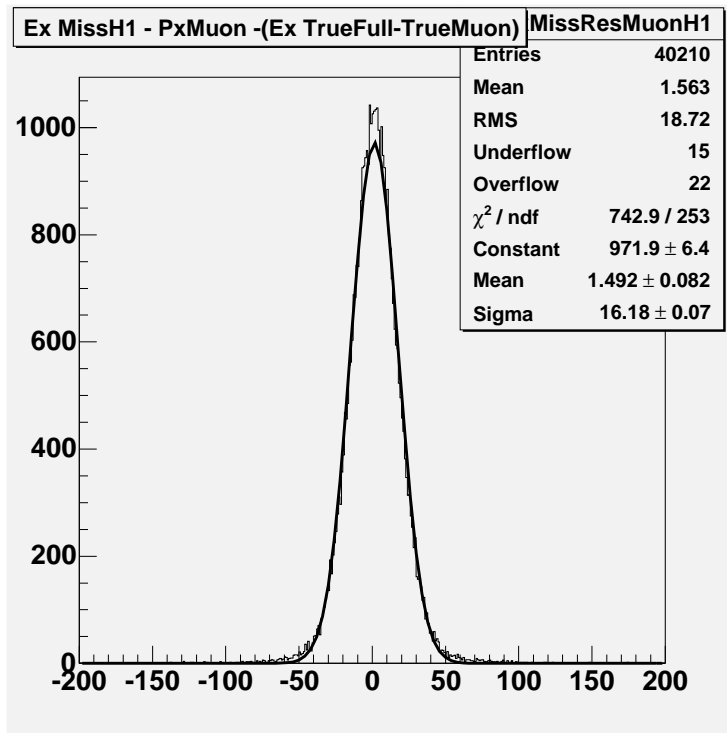


Figure 33: Missing transverse momentum, along X , in $t\bar{t}$ events with exactly one top semi-leptonic decay.

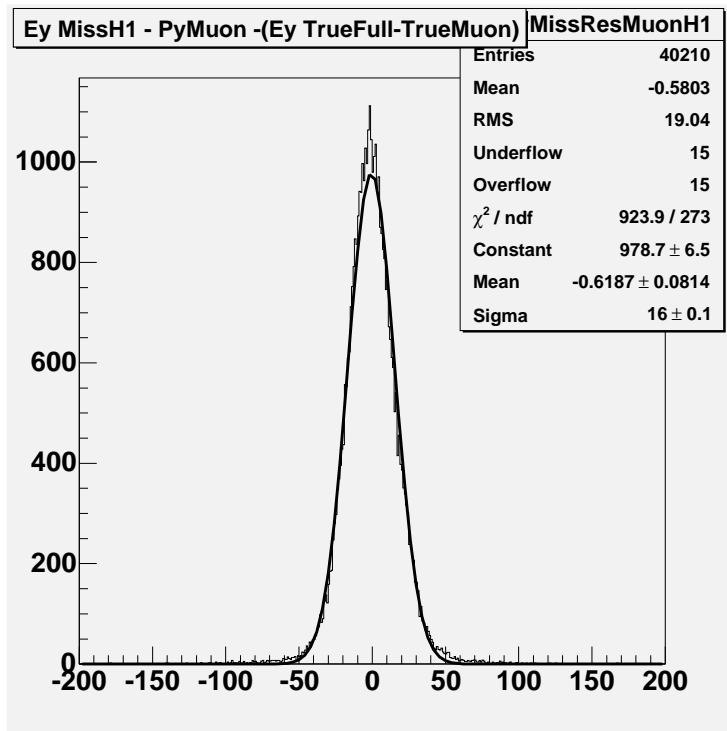


Figure 34: Missing transverse momentum, along Y , in $t\bar{t}$ events with exactly one top semi-leptonic decay.

8.2 The lepton-missing p_T transverse mass

Considering events with exactly one isolated lepton of $p_T > 20$ GeV/c, we form the leptonic transverse mass using the usual formula and neglecting particle masses:

$$M_t = \sqrt{2. * (E_t^\nu * E_t^l - (p_x^\nu * p_x^l + p_y^\nu * p_y^l))}$$

Figure 35 and Figure 36 show the obtained transverse masses for electron and muon events which have to be compared to the expected distribution of Figure 37. In this figure we have used p_x and p_y summed over all neutrinos in the event having $|\eta| < 3.2$. The tail observed well above the Jacobian peak is due to events with more than one neutrino (top semi-leptonic decay followed by a b semi-leptonic, or double semi-leptonic top decays).

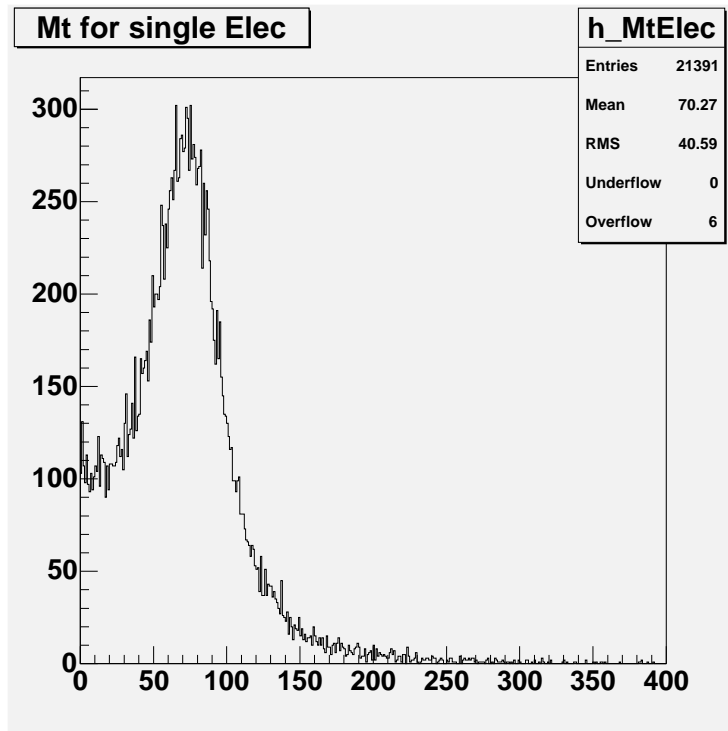


Figure 35: Reconstructed transverse mass for events with one isolated electron

Selecting the events which have only one top semi-leptonic decay we get a transverse mass resolution (see figure 38) of around $16 \text{ GeV}/c^2$ but we observe a systematic $3 \text{ GeV}/c^2$ shift. If we split the sample into electron and muon events (figure 39 and figure 40) we observe that the transverse mass shift is $1 \text{ GeV}/c^2$ larger for muon events than for electron events. In order to investigate this offset we compute the difference of the missing p_T , p_T^{miss} , and the p_T of the generated neutrino, p_T^ν as a function of the missing p_T . As one can see on figure 41, there is a strong dependence on p_T^{miss} , but an independence on the type of lepton. Therefore, we use the same correction of p_T^{miss} for both type of events. In order to translate this correction to missing p_x and missing p_y , we correct the p_T^{miss} amplitude but we keep the direction obtained before correction. We have also investigated the calibration of the leptons. Figure 42 and figure 43 show the resolution on the electron and muon momenta. It is clearly visible that electrons are not perfectly calibrated. Figure 44 shows the reconstructed electron energy minus true electron energy as a function of the reconstructed energy. This mis-calibration, known to exist in version 7.0.0 of ATHENA, is due to the fact that the calibration was performed for photons. Correcting

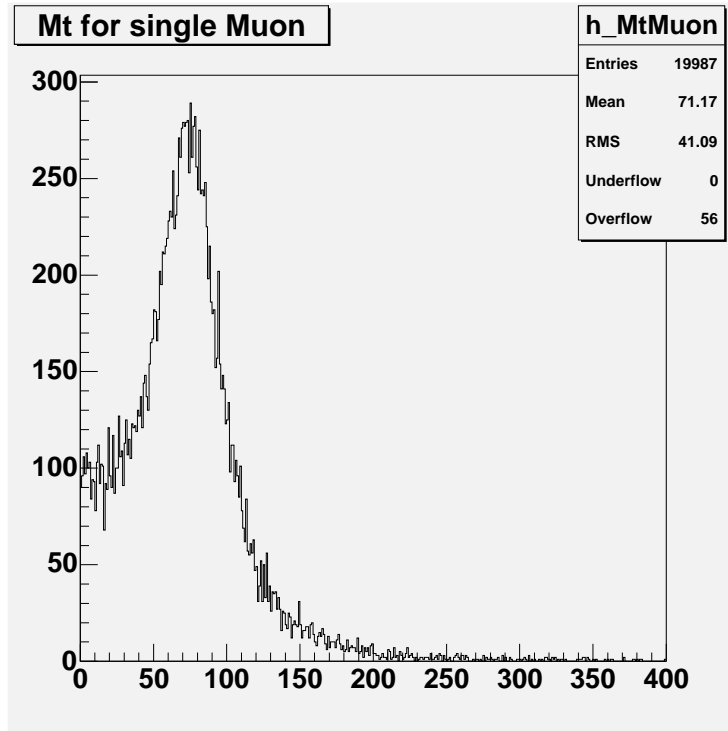


Figure 36: *Reconstructed transverse mass for events with one isolated muon*

for the electron energy mis-calibration reduces the difference between the transverse mass plot obtained with electrons compared to the one obtained with muons. A $0.2 \text{ GeV}/c^2$ differential shift still remains between the two kinds of events. This is probably due to the energy deposited by the muon in the calorimeter which was not subtracted when computing missing p_T . If we now recompute the resolution on the transverse mass we observe that the offset has decreased by a factor 2 (Figure 45) and that the resolution is slightly improved.

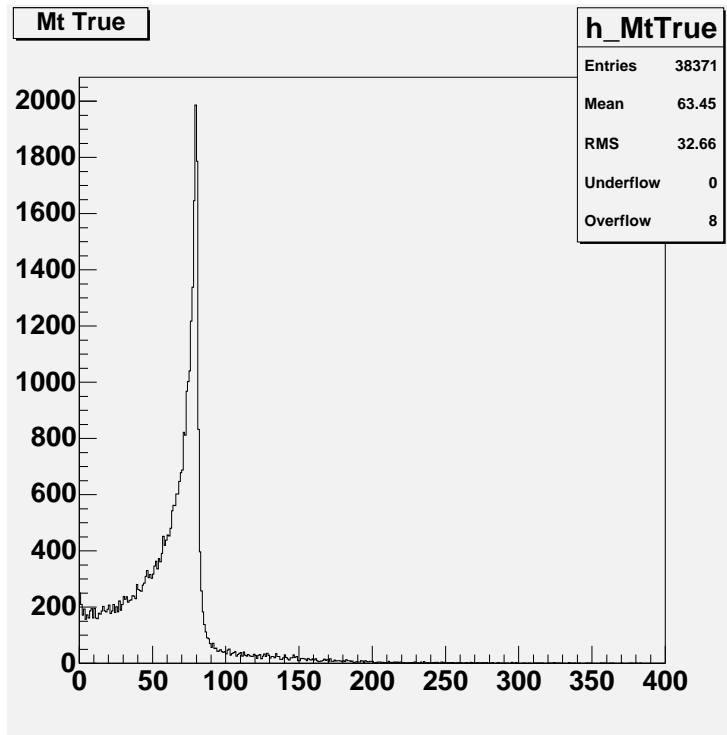


Figure 37: *Generated transverse mass for events with one isolated lepton.*

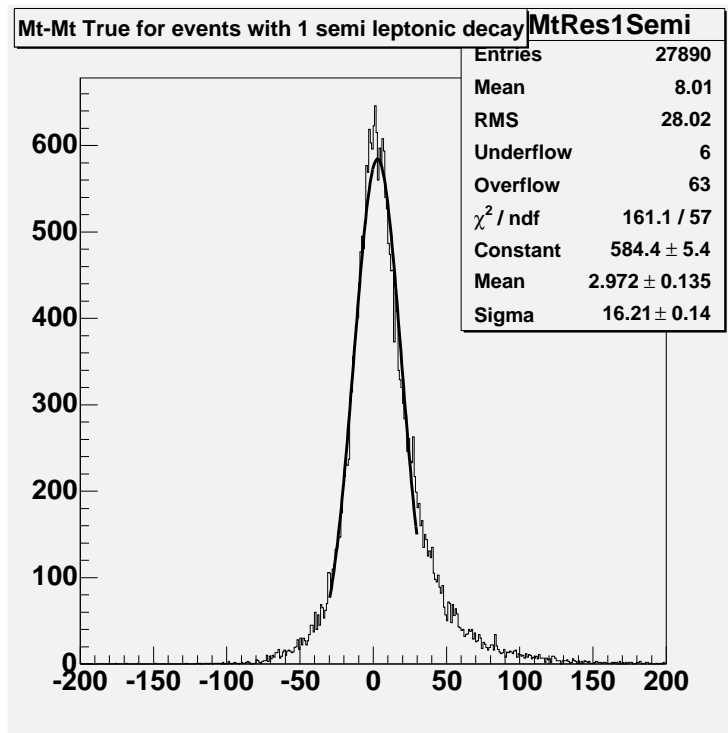


Figure 38: *Reconstructed transverse mass resolution for events with one top quark semi-leptonic decay.*

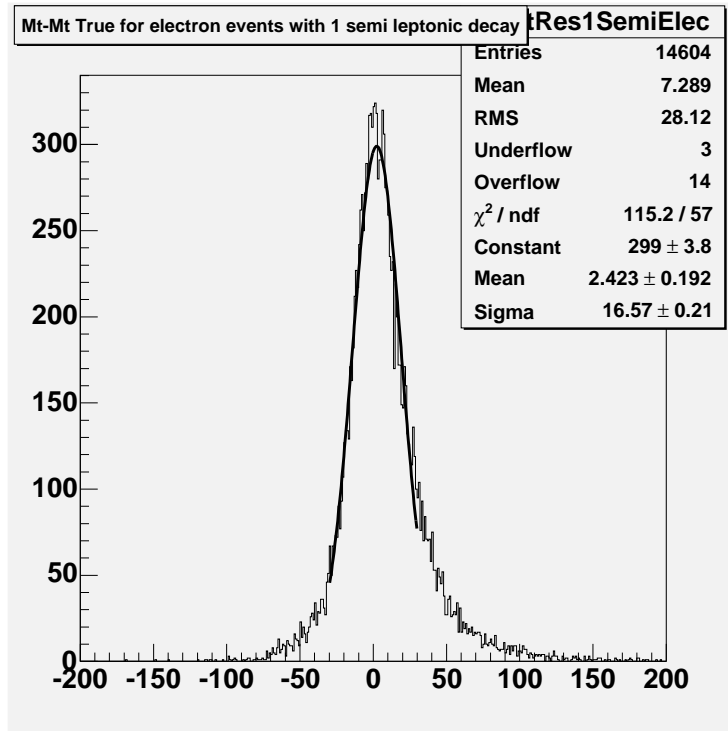


Figure 39: Reconstructed transverse mass resolution for events with one top quark semi-leptonic decay and one isolated electron.

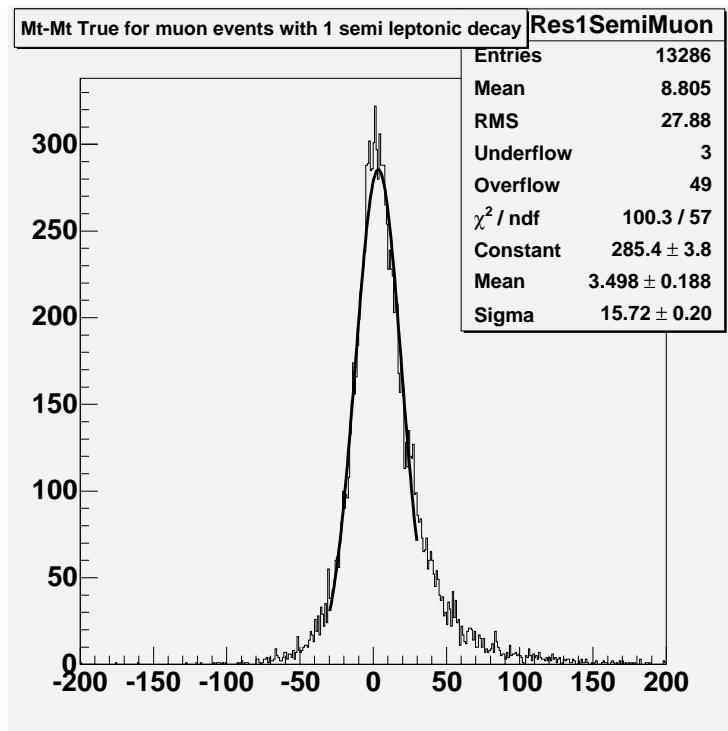


Figure 40: Reconstructed transverse mass resolution for events with one top quark semi-leptonic decay and one isolated muon.

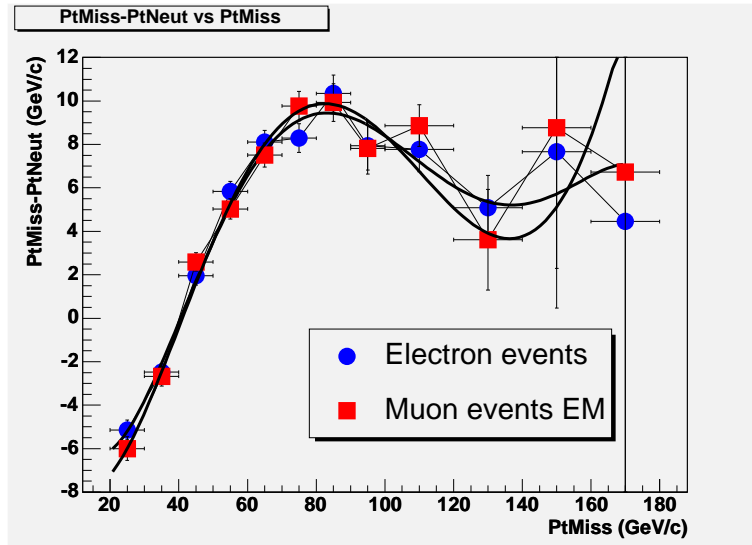


Figure 41: $p_T^{Miss} - p_T^\nu$ as a function of p_T^{Miss} for events with one top quark semi-leptonic decay.

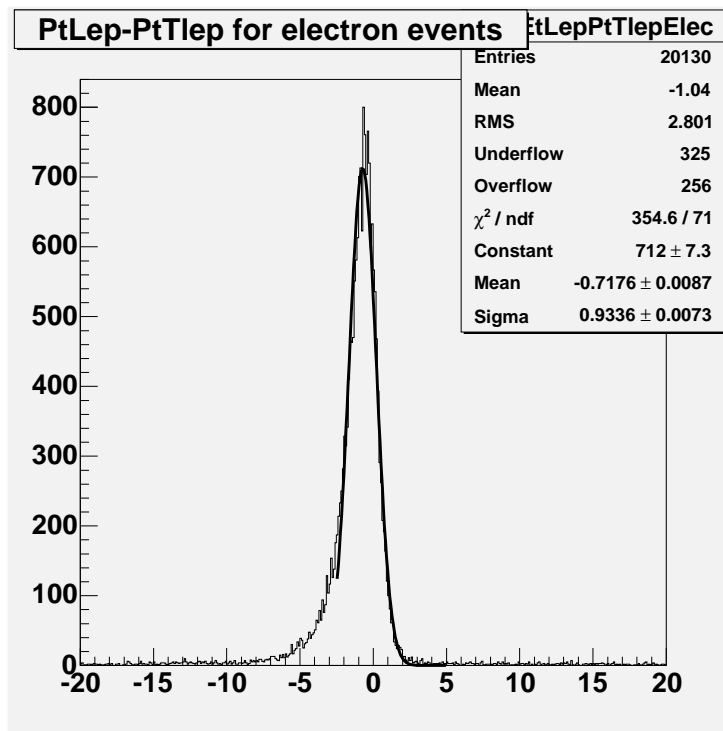


Figure 42: Resolution on the electron momentum.

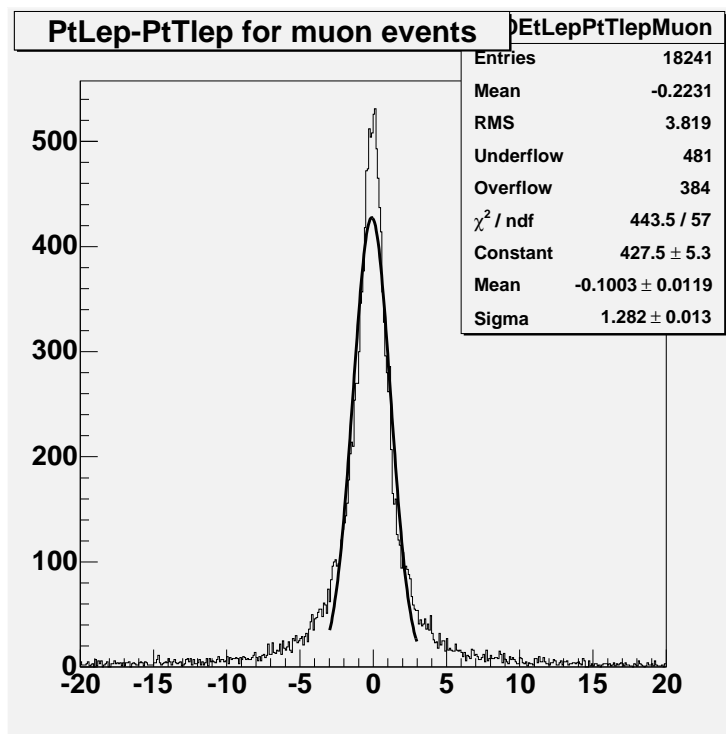


Figure 43: *Resolution on the muon momentum.*

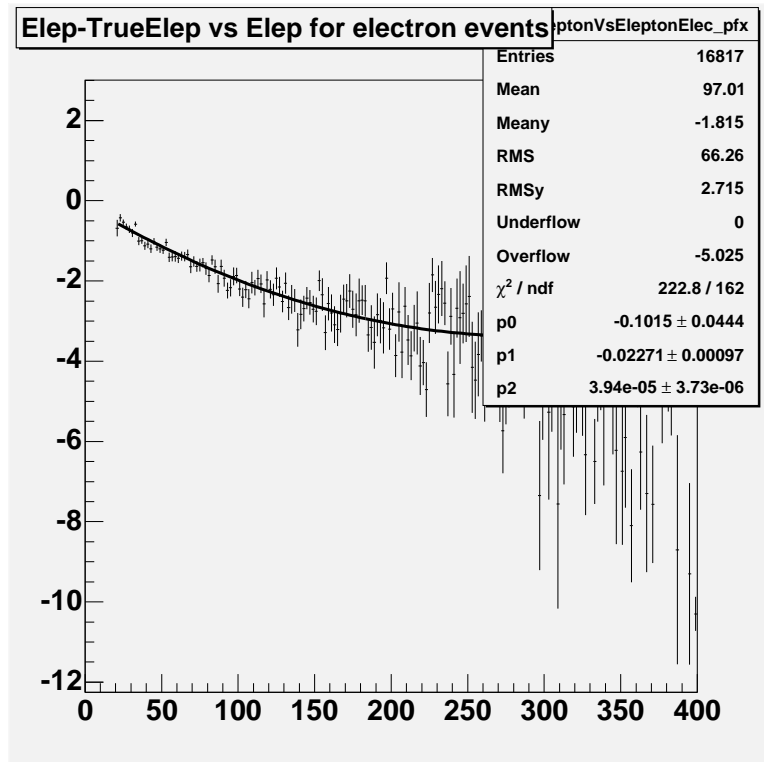


Figure 44: Reconstructed electron energy minus true electron energy as a function of reconstructed energy. The fitted second order polynomial will be used to correct the electron energy.

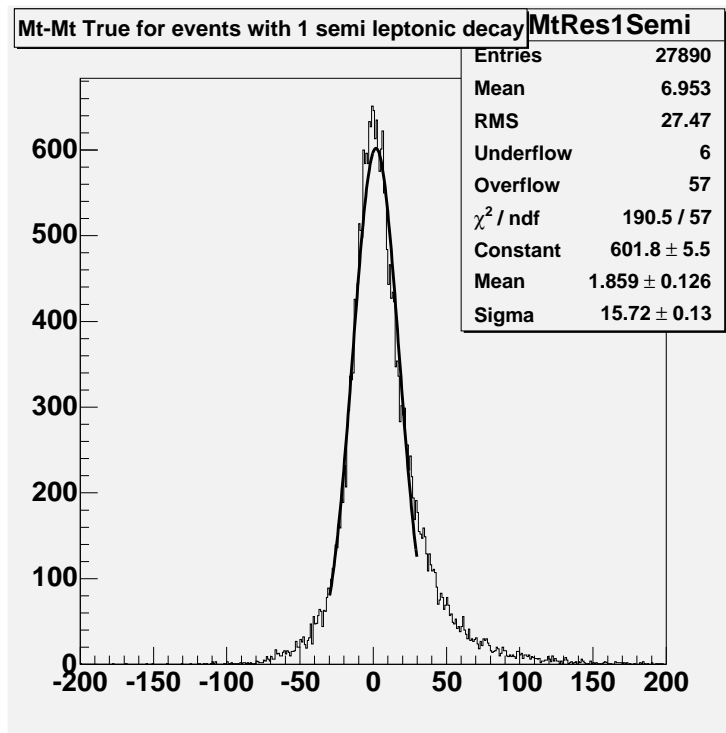


Figure 45: Reconstructed transverse mass resolution for events with one top quark semi-leptonic decay after p_T^{Miss} calibration.

8.3 Reconstruction of the neutrino p_z

Using the known W mass, the reconstructed lepton and the missing p_T components we can write the W mass as a function of neutrino p_z using the following equation:

$$M_W^2 = m_l^2 - 2 * (p_x^l * p_x^\nu + p_y^l * p_y^\nu) + 2 * E_l * \sqrt{((p_T^{Miss})^2 + (p_z^\nu)^2)} - 2 * (p_z^l * p_z^\nu)$$

Unfortunately the equation is not linear in neutrino p_z^ν . The equation has no solution when the neutrino-lepton transverse mass is above the W mass, due to energy resolution. In the other cases we usually find two valid solutions (one with positive $p_z^{\nu Rec}$ and one with negative $p_z^{\nu Rec}$). Therefore, we have either two reconstructed leptonic W's or none. In order to estimate the obtained resolution we use the true neutrino p_z (p_z^ν) to choose among the two solutions. The obtained resolution is around 30 GeV/c but with rather long non gaussian tails (see figure 46).

Due to the resolution on p_T^{miss} , the transverse mass jacobian peak is widened. In our W mass constraint we therefore reject all events having a transverse mass above the W mass. Part of these events can be recovered assuming $p_z^{\nu Rec} = 0$ and imposing M_W^{Rec} below 100 GeV/c². The obtained $p_z^{\nu Rec}$ resolution seems rather reasonable (Figure 47). We decide to add these events to the sample for which the W mass constraint works. Around 46% of the events have a reconstructed neutrino p_z .

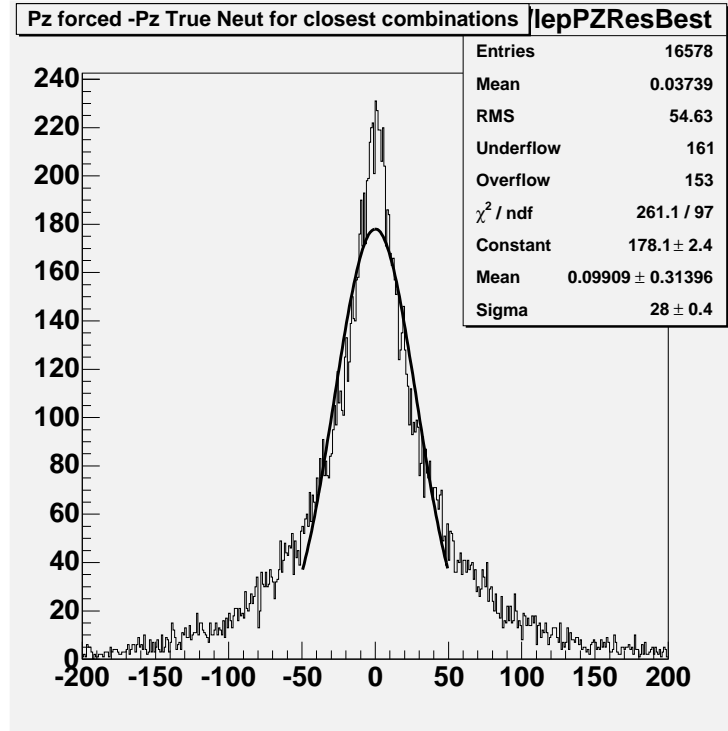


Figure 46: Distribution of forced $p_z^{\nu Rec} - p_z^\nu$ for the solution of minimal difference.

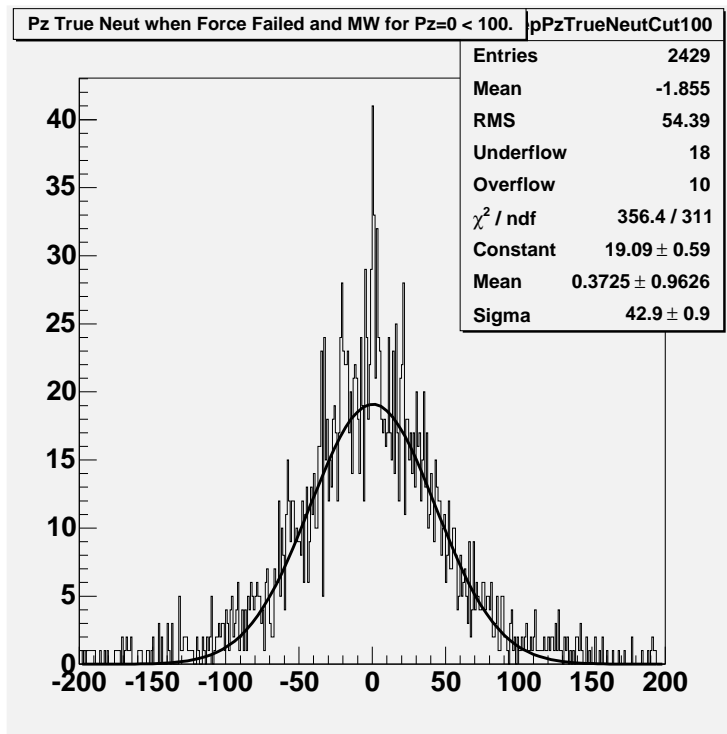


Figure 47: Distribution of p_z^ν for events having a lepton-missing p_T transverse mass larger than M_W . Assuming that $p_z^{\nu Rec} = 0$ we select the events having $M_W^{Rec} < 100 \text{ GeV}/c^2$

9 The semi-leptonic top quark mass reconstruction

9.1 Combining the leptonic W with a b quark jet

To reconstruct the top mass on the leptonic side, we have to associate the leptonic W with one of the two possible b quark jets. To study the quality of the association we will consider all reconstructed leptonic W candidates. We have considered three association methods:

- Maximizing the top quark transverse momentum.
- Minimizing the angle between the lepton and the b quark jet.
- Minimizing the angle between the leptonic W and the b quark jet.

As for the hadronic side, the best method (see figure 48) is the one which maximises the P_t of the top quark. The obtained b jet association purity is comparable to the one of the hadronic side.

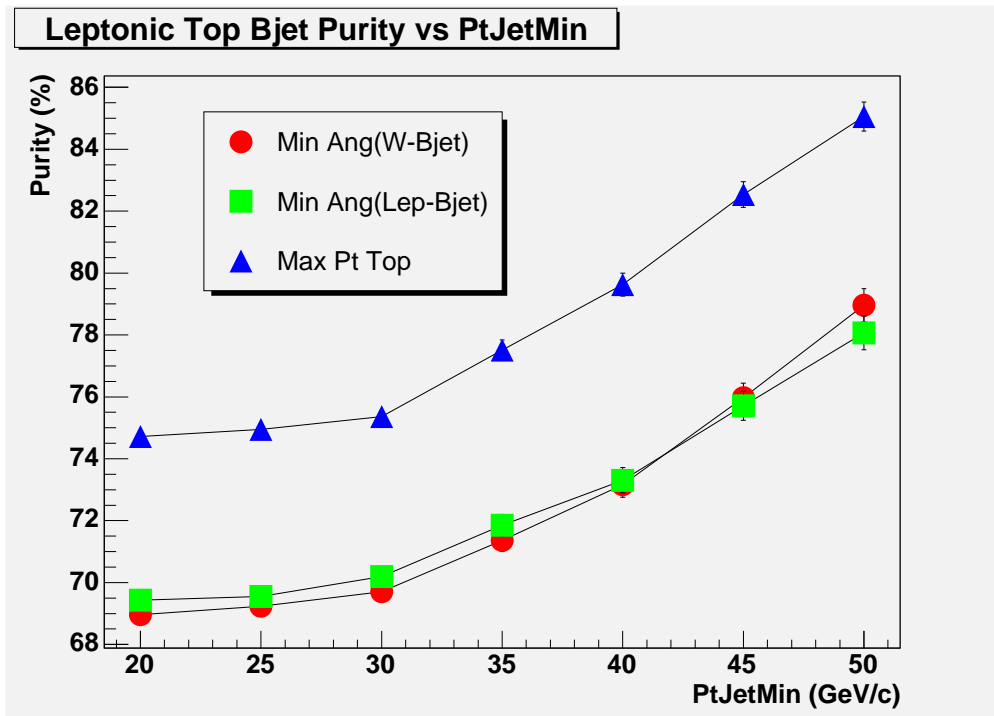


Figure 48: B jet association purity on the semi-leptonic decay top quarks as a function of cut on jet p_T .

9.2 Results on the reconstructed semi-leptonic top quark mass

Figure 49 shows the top mass obtained on the leptonic side for a cut on the jet p_T of 40 GeV/c, for all leptonic W candidates. When we keep only the top mass closest to the generated one (Figure 50) the agreement between the generated and reconstructed mass improves by 1.4 GeV/c² and the resolution is of the order of 17 GeV/c². The dependence of the mass on the cut on the jet p_T is shown in figure 51. The sensitivity to the jet p_T cut is less important than for the hadronic side since there is only one jet entering the mass computation. Nevertheless the width is much larger and the mass stays systematically below the generated one. Figure 52 shows the obtained event selection efficiency as a function of the cut on the jet p_T . The efficiency is slightly higher than for the hadronic side.

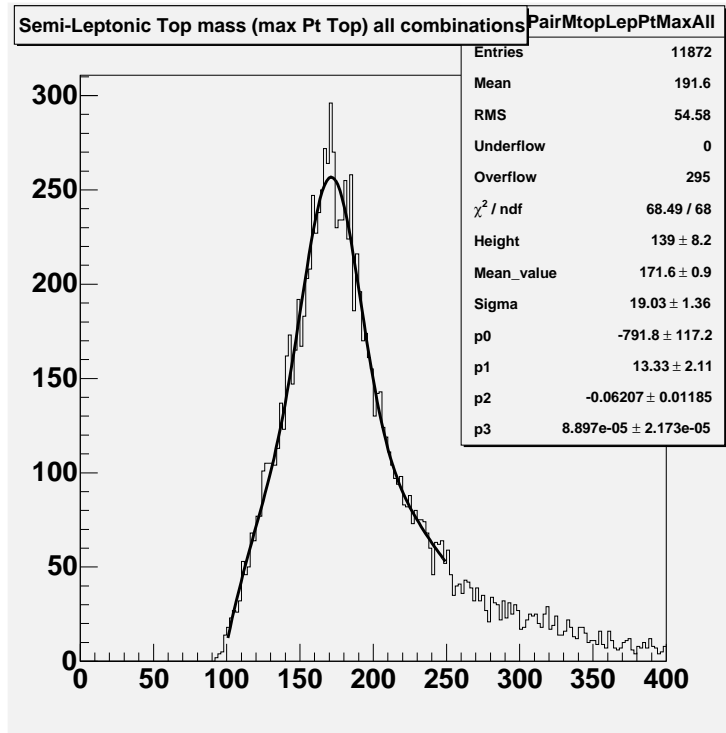


Figure 49: Reconstructed semi-leptonic top quark mass keeping all leptonic W candidates and for a p_T cut of 40 GeV/c. The mass has been fitted using a gaussian plus a third order polynomial.

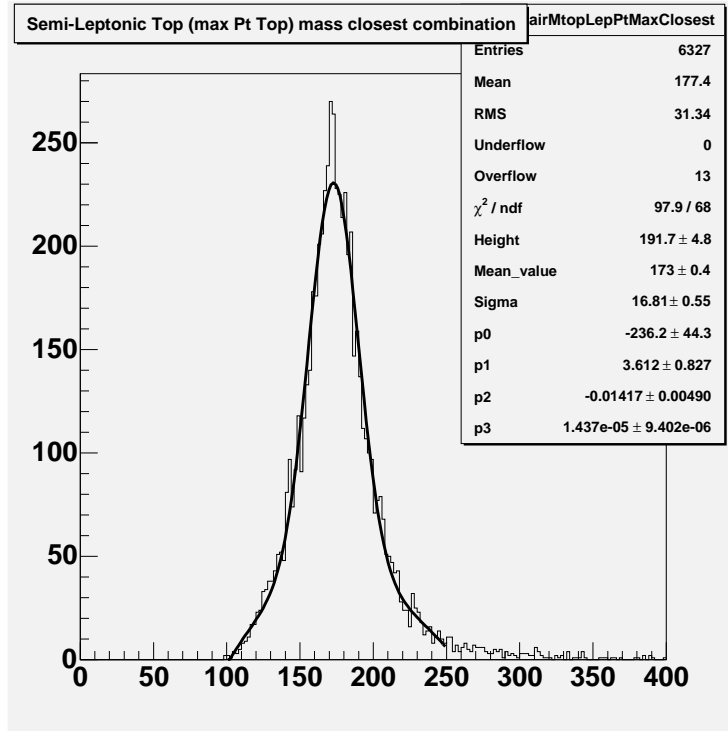


Figure 50: Reconstructed semi-leptonic top quark mass selecting the leptonic W candidates giving the top mass closest to the generated one ($175 \text{ GeV}/c^2$). A p_T cut of $40 \text{ GeV}/c$ has been applied. The mass has been fitted using a gaussian plus a third order polynomial.

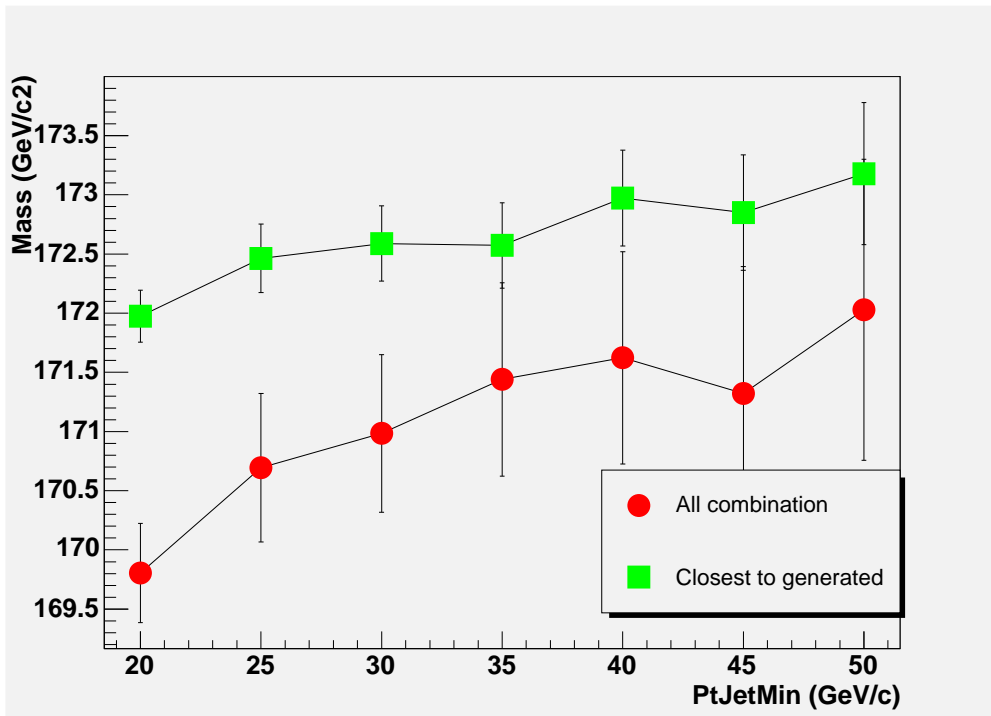


Figure 51: Reconstructed leptonic top mass as a function of the cut on the jet p_T .

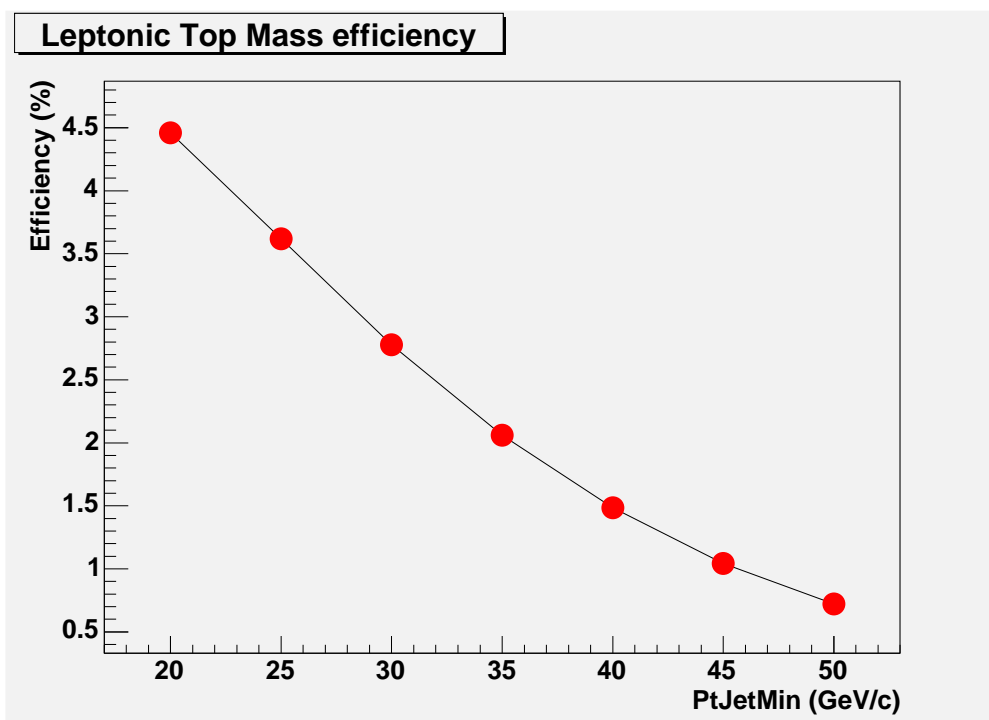


Figure 52: *Event section efficiency as a function of the cut on the jet p_T .*

9.3 Sensitivity to generated top quark mass

In this section we present the reconstructed semi-leptonic top quark mass for three different generated masses ($160 \text{ GeV}/c^2$, $175 \text{ GeV}/c^2$ and $190 \text{ GeV}/c^2$). The dependence of the reconstructed mass on the jet p_T cut observed at $175 \text{ GeV}/c^2$ has not been corrected. Figure 53 shows the reconstructed semi-leptonic top quark mass (considering all combinations) as a function of the generated mass for a jet p_T cut of $40 \text{ GeV}/c$. We observe that the systematic negative bias increases with the generated mass. In principle part of this effect as well as the dependence on the jet p_T cut can be corrected using a toy Monte-Carlo like ATLFAST. This study remains to be performed.

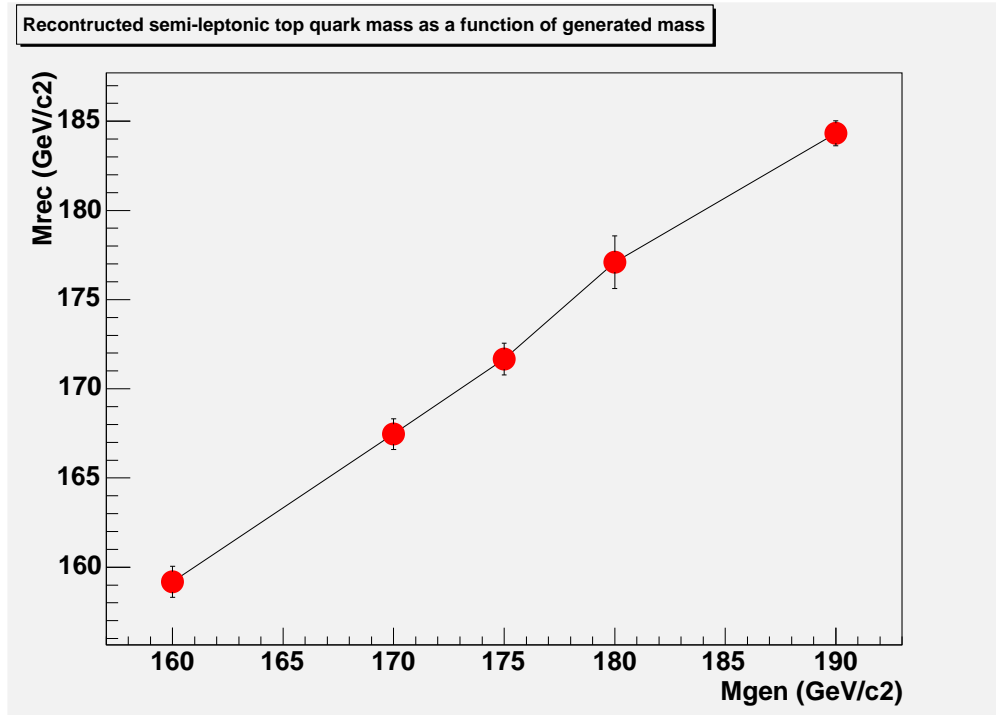


Figure 53: Reconstructed semi-leptonic top quark mass (considering all combinations) as a function of the generated mass for a jet p_T cut of $40 \text{ GeV}/c$.

Part IV

Combining both top decays

In this part we try to improve on both top mass measurements by combining the hadronic and the semi-leptonic top quark decays. The goals are first to solve the semi-leptonic side ambiguity and second to improve on the b jet association purity on both sides. We first proceed with the study for a generated top mass of $175 \text{ GeV}/c^2$ before studying the other generated top mass samples.

10 Combining the W's with the b quark jets

To reconstruct the top masses we have to associate the W's with the b quark jets. On the semi-leptonic side we have mostly two W candidates. In order to solve the ambiguity we use the mass difference between the hadronic and the semi-leptonic sides. We have considered the three following methods to associate the b quark jets:

- 1) Minimize $\Delta m = \left| M_{\text{top}}^{\text{Had}} - M_{\text{top}}^{\text{Lep}} \right|$ to choose at the same time the b quark jet and the leptonic W. The mass difference of the selected top pairs shown on figure 54 is well centered at zero with a sigma of the order of $23 \text{ GeV}/c^2$. This can be done because the mass resolution is much larger than the natural top width.
- 2) Combine the b jets with the W's in order to maximize the top quark p_T independently on both sides and choose the leptonic W minimizing Δm . If no leptonic W has been reconstructed the hadronic mass is still kept.
- 3) We first use method 2. If we have a conflict in the b quark jet association (one b jet is used twice) or if the mass difference is really large (above $70 \text{ GeV}/c^2$) we consider that the association is probably wrong and we use method 1 for these events.

Figure 55 and figure 56 show the b jet purity obtained for both types of top quark decays as a function of the cut on the jet p_T . It is clearly visible that on the hadronic side the first method is the most efficient for jet p_T below $30 \text{ GeV}/c$ whereas method 3 is better above. On the leptonic side method 3 is always better. For this reason method 3 will be used for further analysis.

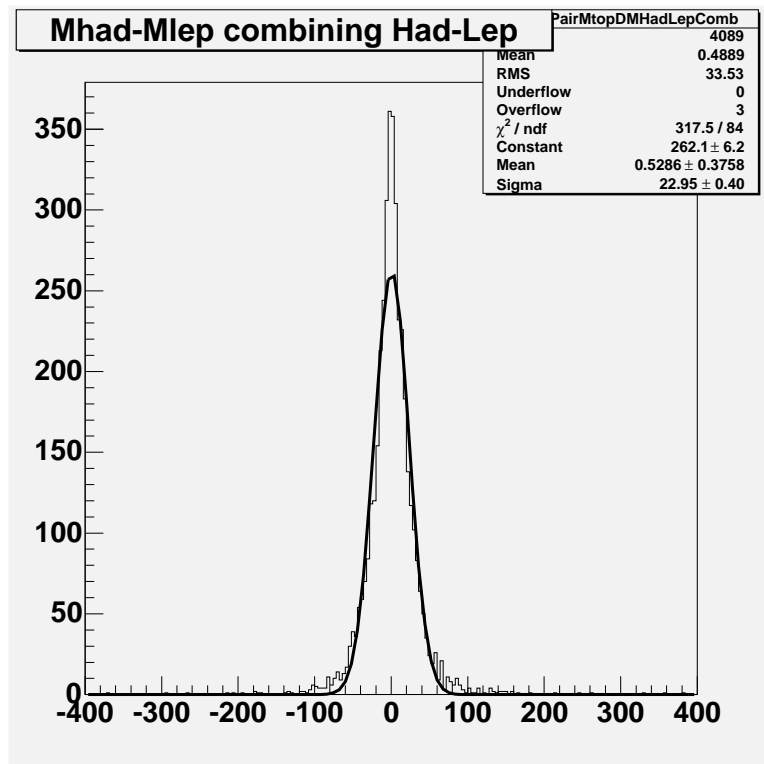


Figure 54: Mass difference of the selected top pairs using method 1.

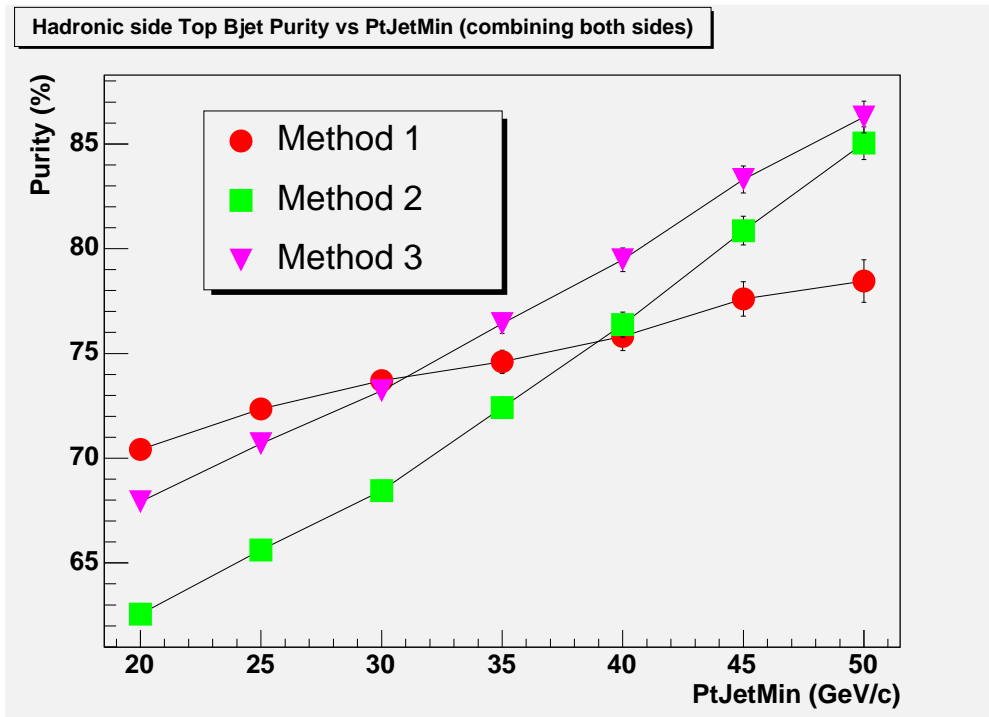


Figure 55: *B* quark jet purity on the hadronic side as a function of the cut on the jet p_T .

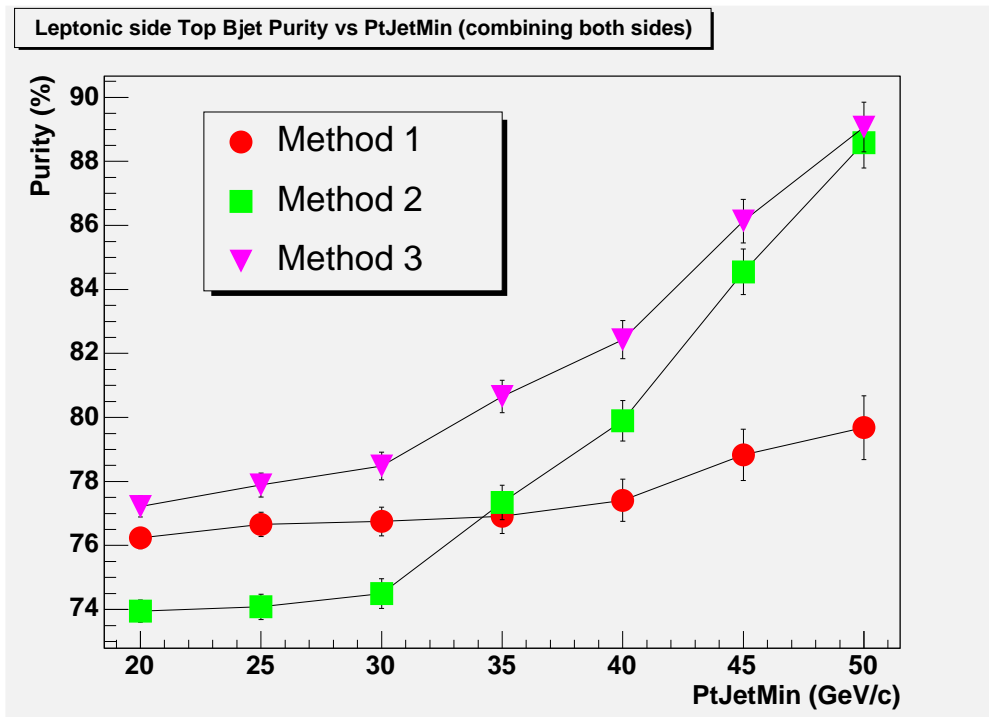


Figure 56: *B* quark jet purity on the semi-leptonic side as a function of the cut on the jet p_T .

11 Results on the reconstructed top quark mass

Figure 57 shows the reconstructed top quark masses for both types of top quark decays as a function of the cut on the jet p_T . The behaviour of the reconstructed top mass as a function of p_T is different on both sides but at high p_T jet cut the masses become comparable. This systematic difference has to be investigated, for example by comparing to a toy Monte-Carlo simulation. Figure 58 and figure 59 show the mass distributions obtained for both types of decay and a p_T jet cut of 40 GeV/c. Figure 60 and Figure 61 show the obtained top quark masses for a p_T jet cut of 40 GeV/c as a function of the generated mass. The reconstructed masses behave linearly with the generated mass but with a different slope for the hadronic decay than for the leptonic one. Trying to investigate the origin of this difference we have varied both the missing p_T and lepton p_T cuts without observing any significant changes. We suppose that this difference is intrinsic to the method and plan to investigate further using a toy Monte-Carlo simulation.

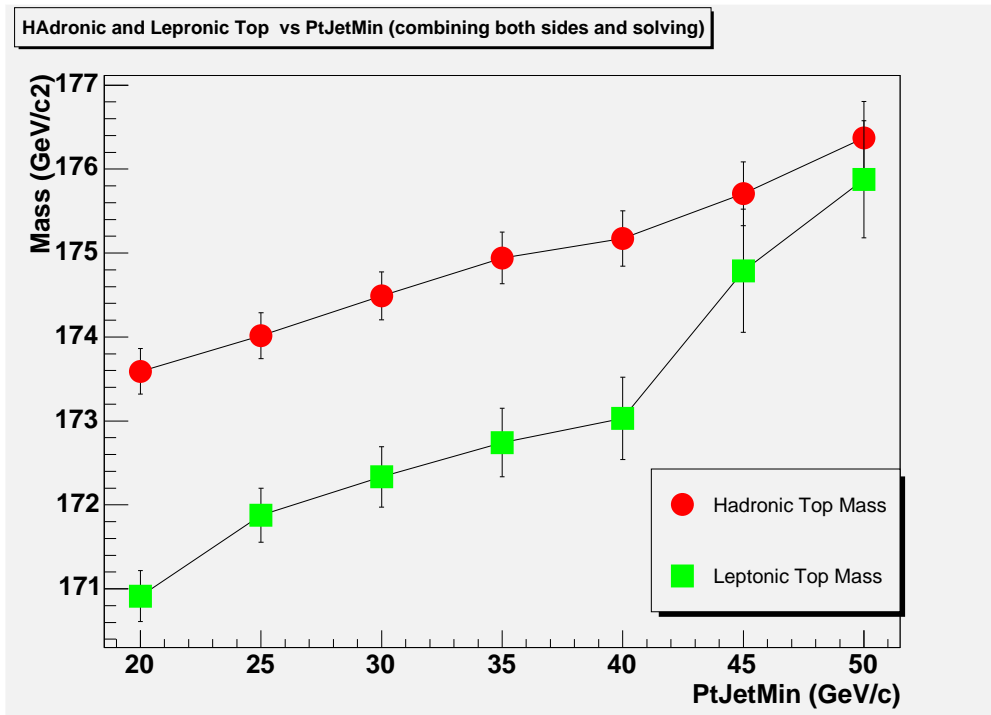


Figure 57: Hadronic and semi-leptonic reconstructed top quark masses using method 3 as a function of the cut on the jet p_T .

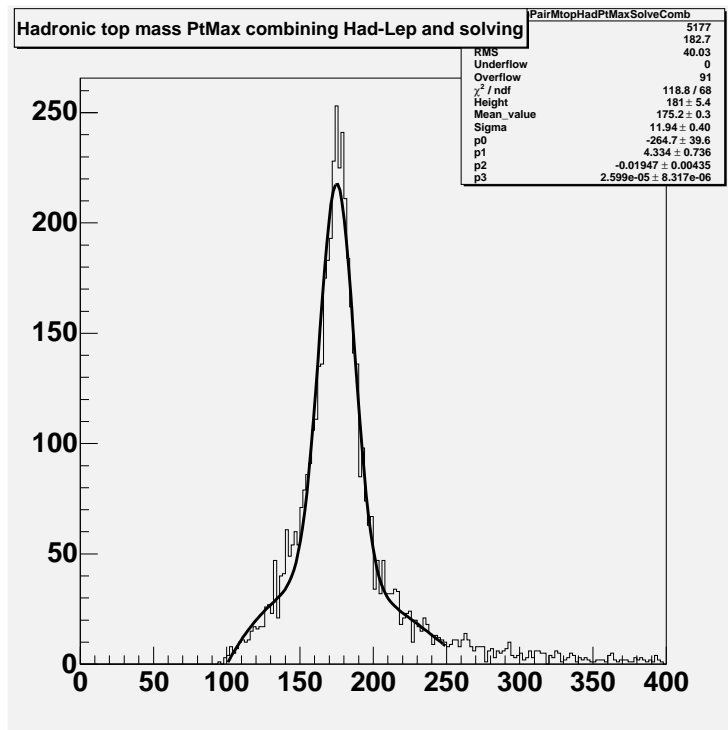


Figure 58: Reconstructed combined hadronic top quark mass for a p_T cut of $40 \text{ GeV}/c$. The mass has been fitted using a gaussian plus a third order polynomial.

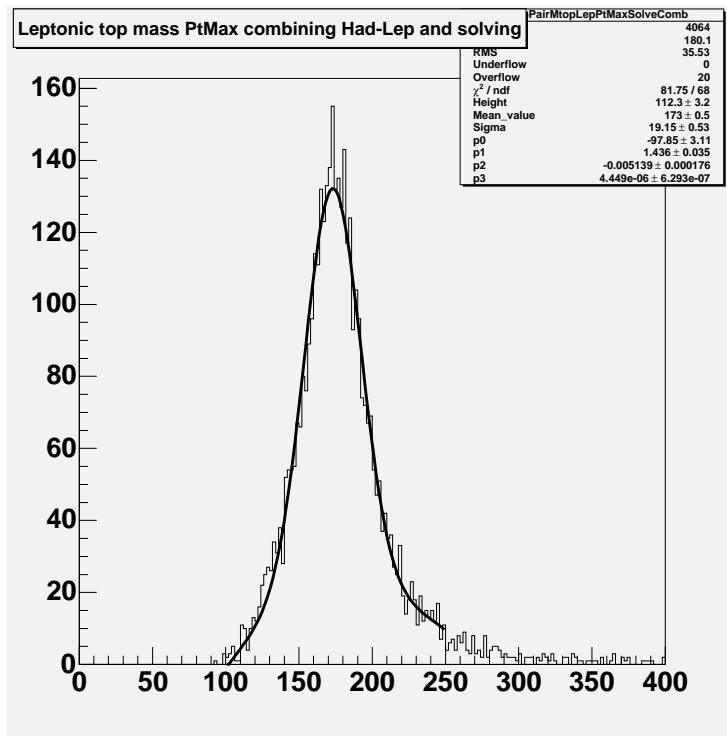


Figure 59: Reconstructed combined semi-leptonic top quark mass for a p_T cut of $40\text{GeV}/c$. The mass has been fitted using a gaussian plus a third order polynomial.

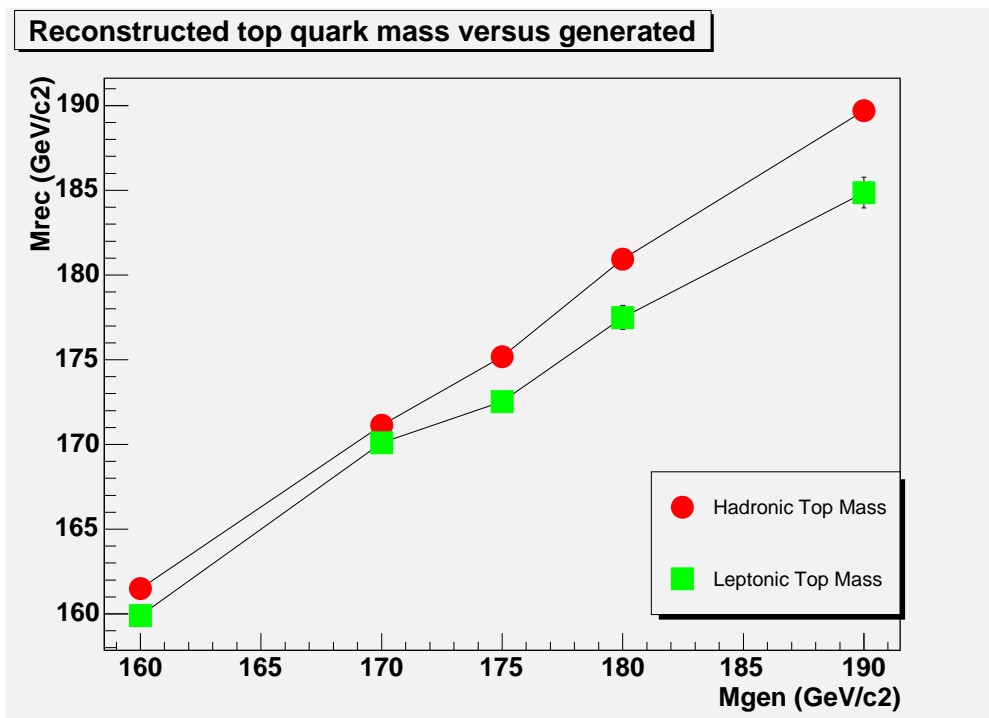


Figure 60: Reconstructed combined top quark mass versus generated mass for a p_T cut of $40\text{GeV}/c$.

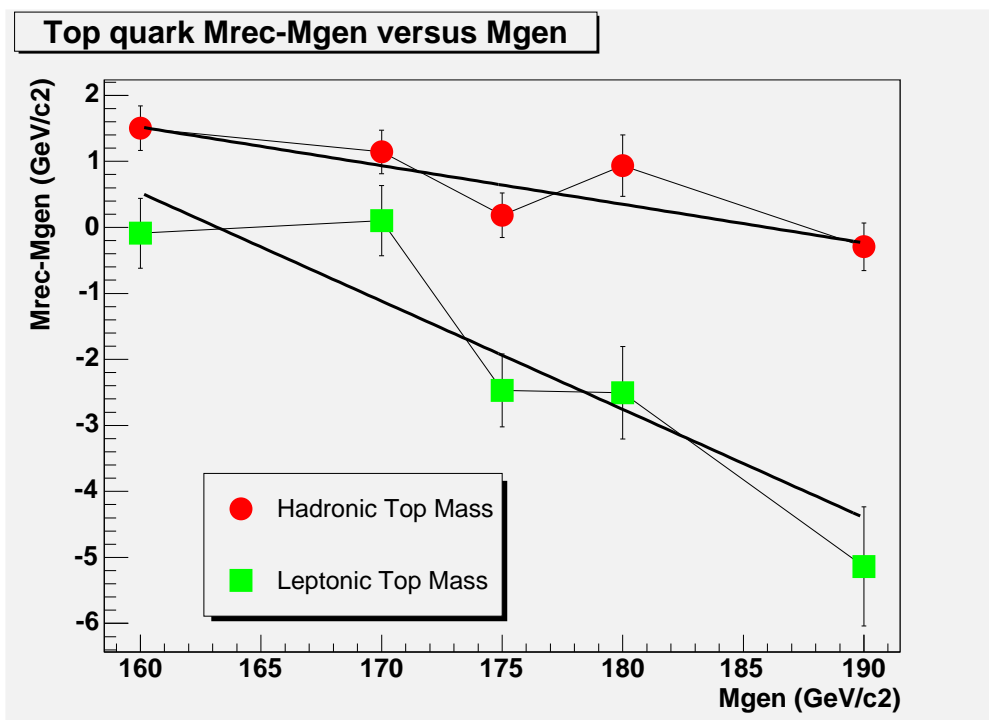


Figure 61: Reconstructed minus generated combined top quark mass versus generated mass for a p_T cut of $40 \text{ GeV}/c$.

Part V

Conclusion

We studied the top mass reconstruction in $t\bar{t} \rightarrow l\nu bjjb$ events using full simulation and reconstruction of this process. Both the $l\nu b$ and jjb decays were considered, for five generated top masses (160, 170, 175, 180 and 190 GeV/c^2). A few sources of systematic errors have been studied.

The resolution on the top mass is about 12 GeV/c^2 for the jjb side (19 GeV/c^2 for the $l\nu b$ side). With these resolutions, the statistical error on the top mass after one week at $10^{33} \text{ cm}^{-2} \text{ s}^{-1}$ is 0.4 GeV/c^2 (0.9 GeV/c^2). The statistical uncertainty will quickly become negligible compared to the uncertainties related to the jet scale determination, which amount to 600 MeV per percent miscalibration for b jets, and to 200 MeV per percent miscalibration for light jets.

In both decay modes, the reconstructed mass exhibits a dependence with the cut on the jet energies due to resolution effects. However, with a fixed cut at $P_T = 40 \text{ GeV}/c$ and if the jet energies are properly calibrated, the mass reconstructed in the hadronic side is very close to the generated mass, for the full mass range.

In the semi-leptonic side, the reconstructed mass tends to be smaller than the generated mass. Although this effect remains to be understood, the leptonic side can be used to increase the purity of the b association on the hadronic side.

This analysis will be redone with ATHENA 10.0.1, which will allow in particular to use a more realistic b-jet tagging, and to study the impact of jet calibration in more detail.

Part VI

Annex

12 Appendix 1: Electron identification.

In order to identify electrons we consider electron-gamma candidates and check the additional criteria defined below.

Looking into the CBNT e-gamma data block, we first select clusters having the `eg_IsEM` flag set to zero. This guarantees that both the longitudinal and the lateral shower profiles are compatible with an electromagnetic shower. Then we request that at least one reconstructed track is found in front of the cluster. Finally we cut on the distance between the cluster and the closest track both in eta and phi. Because of the magnetic field the bremsstrahlung effects arises always only on one side in phi of the cluster. For this reason the e-gamma data block contains the signed track-cluster phi difference (Figure 62) and our identification cut is asymmetric.

In order to define the track-cluster matching cuts we have generated single electron samples for different energies. The $\Delta\eta$ cut has been studied as a function of the electron energy such as the efficiency stays constant at 95% (Figure 63). The $\Delta\phi$ cut has been studied as a function of the electron transverse energy such as the cut on both sides has a 95% constant efficiency (Figure 64 and Figure 65).

The effect on the electrons identification efficiency of the previous cuts is shown on Figure 66. The large drop at low energy is mainly due to the fact that the electrons were generated flat in η and with a constant energy but that the minimal cluster transverse energy was set to the default (5 GeV/c).

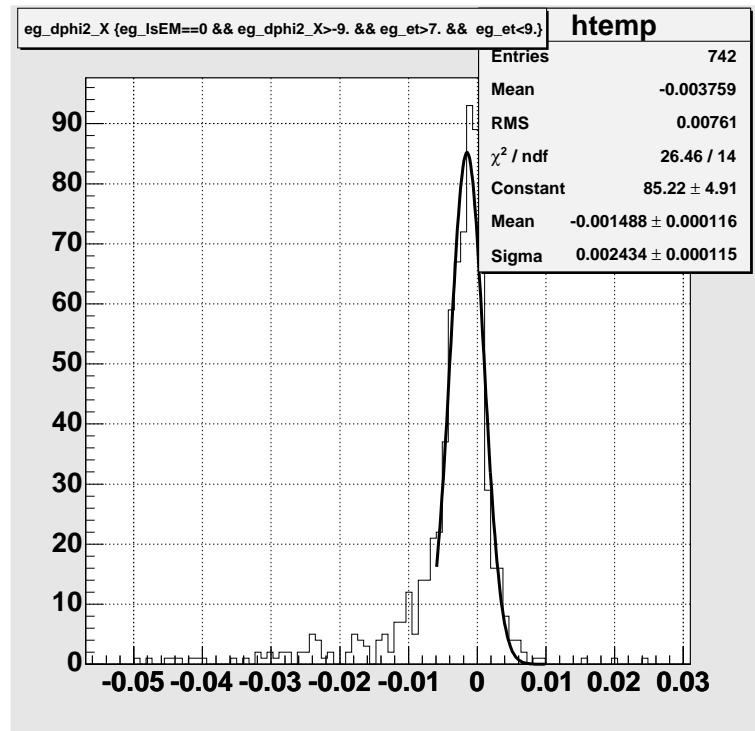


Figure 62: Signed distance track-cluster in phi for electrons having a transverse energy between 7 GeV/c and 9 GeV/c.

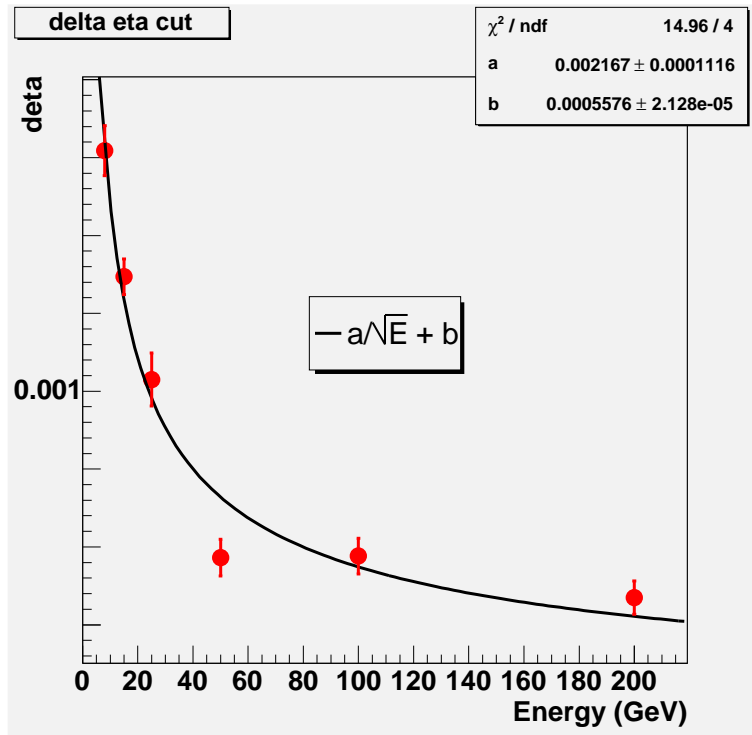


Figure 63: *Delta eta electron identification cut as a function of the electron energy.*

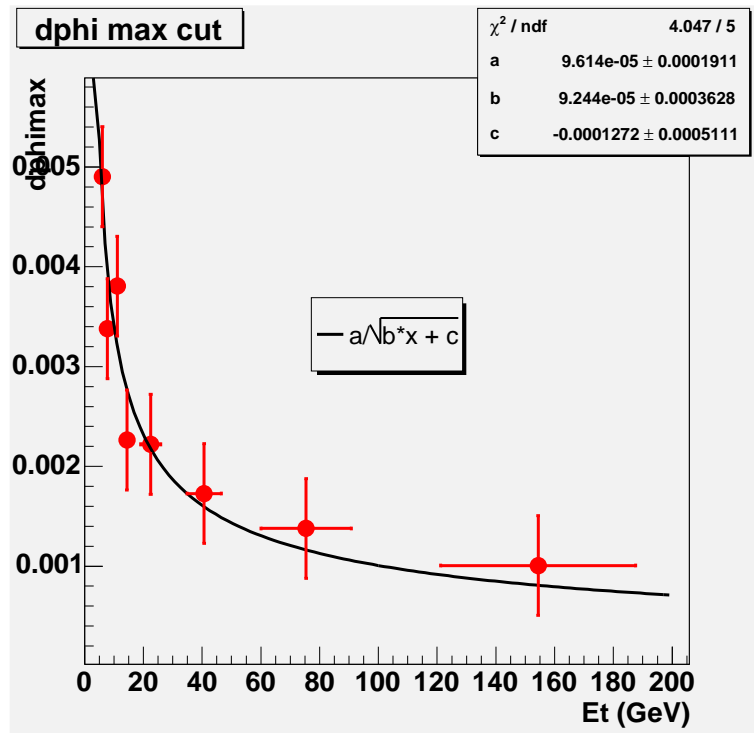


Figure 64: *Positive delta phi electron identification cut as a function of the electron transverse energy.*

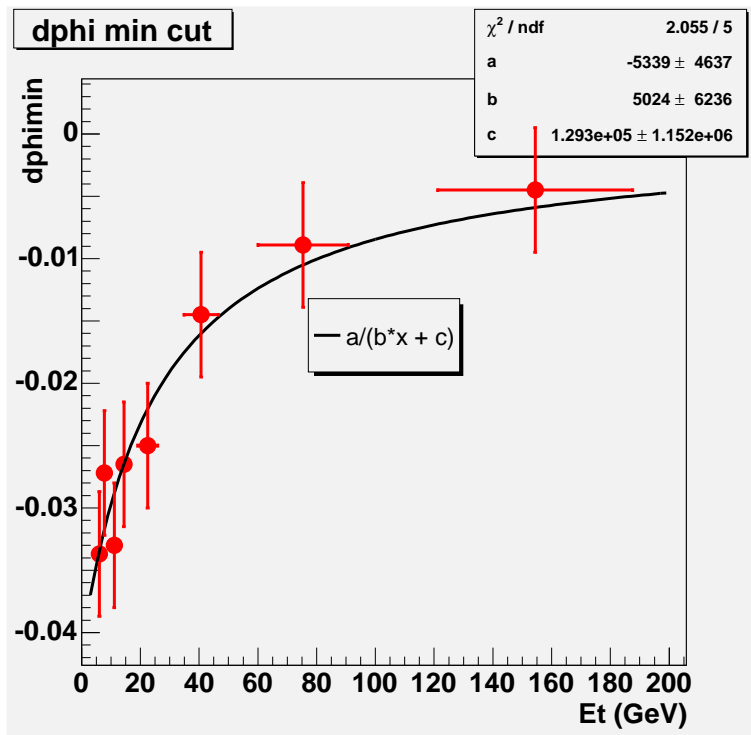


Figure 65: Negative delta phi electron identification cut as a function of the electron transverse energy.

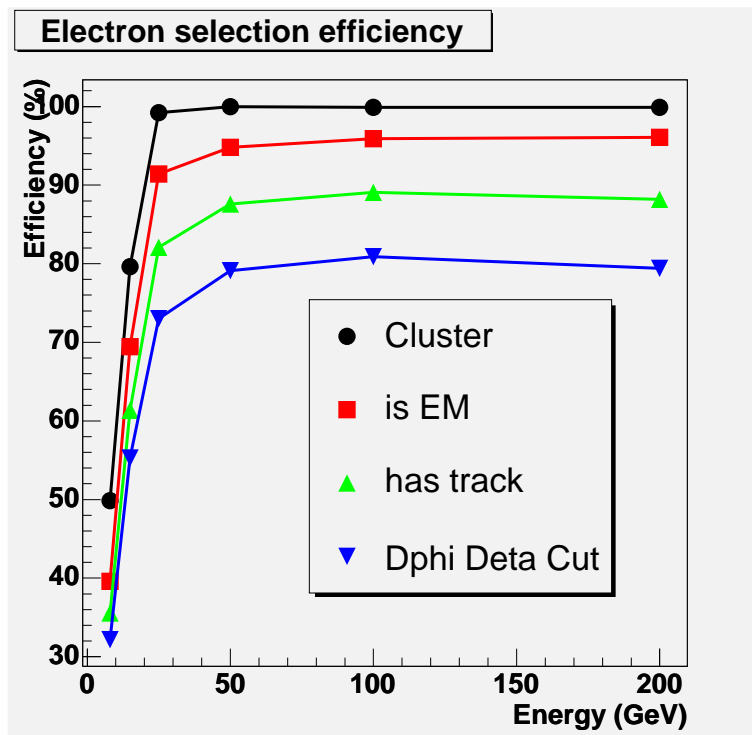


Figure 66: Electron selection combined efficiency for the different cuts as a function of the electron energy.

References

- [1] **I.Borjanovic et al.** , **hep-ex/0403021**

- [2] **ATLAS Collaboration** , ATLAS Detector and Physics Performance Technical Design Report, **CERN-LHCC-99-14-15**